Capillary Filling Dynamics of Polymer Melts in a Bicontinuous Nanoporous Scaffold

Weiwei Kong^{1†}, Anastasia Neuman^{2‡}, Aria C. Zhang¹, Daeyeon Lee², Robert A. Riggleman², Russell J. Composto¹

1: Department of Materials Science and Engineering, University of Pennsylvania, Philadelphia,

PA

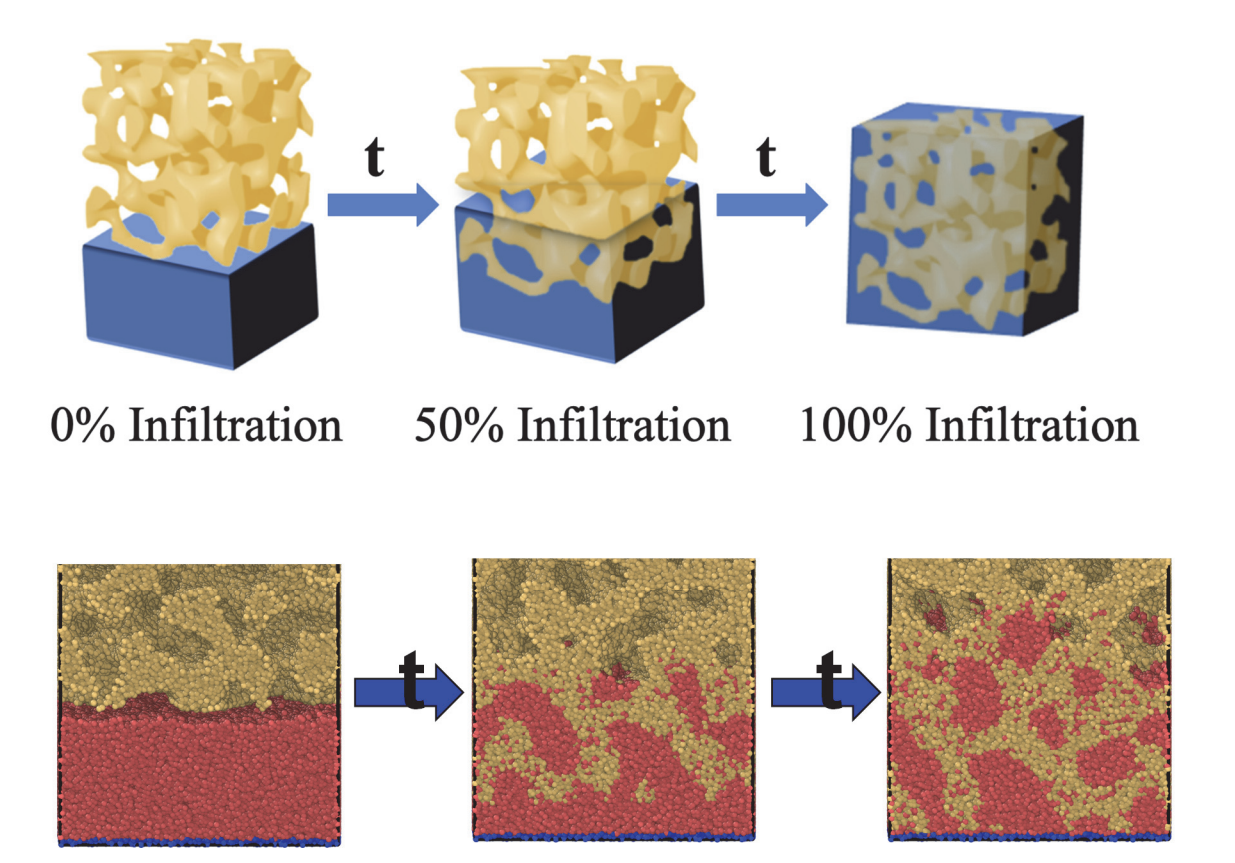
2: Department of Chemical and Biomolecular Engineering, University of Pennsylvania,

Philadelphia, PA

‡: these authors contributed equally

Abstract

Polymer infiltrated nanoporous gold (PING) is prepared by infiltrating polymer melts into a bicontinuous, nanoporous gold (NPG) scaffold. Polystyrene (PS) films with molecular weights (M_w) from 424k Da to 1133k Da is infiltrated into a NPG scaffold (ca. 120 nm), with a pore radius (R_n) and pore volume fraction of 37.5 nm and 50%, respectively. The confinement ratios $(\Gamma = \frac{R_g}{R_p})$ range from 0.47 to 0.77, suggesting that the polymers inside the pores are moderately confined. The time for PS to achieve 80% infiltration ($\tau_{80\%}$) is determined using in situ spectroscopic ellipsometry at 150°C. The kinetics of infiltration scales weaker with M_w , $\tau_{80\%} \propto$ $M_w^{1.30\pm0.20}$, than expected from bulk viscosity $M_w^{3.4}$. Further, the effective viscosity of the PS melt inside NPG, inferred from the Lucas-Washburn model, is reduced by more than one order of magnitude compared to the bulk. Molecular dynamics (MD) simulation results are in good agreement with experiments predicting scaling as $M_w^{1.4}$. The reduced dependence of M_w and the enhanced kinetics of infiltration are attributed to a reduction in chain entanglement density during infiltration and a reduction in polymer-wall friction with increasing polymer molecular weight. Compared to the traditional approach involving adding discrete particles into the polymer matrix, these studies show that nanocomposites with higher loading can be readily prepared, and that kinetics of infiltration are faster due to polymer confinement inside pores. These films have potential as actuators when filled with stimuli-responsive polymers as well as polymer electrolyte and fuel cell membranes.



Introduction

Polymer nanocomposites (PNCs) have been widely studied in academic, national and industrial laboratories 1-3. PNCs are broadly defined as a mixture of an inorganic nanofiller dispersed within a polymeric matrix, resulting in a material with properties that the individual components would not exhibit by themselves. PNCs have been utilized in applications involving gas separation membranes ^{4,5}, optically responsive devices ⁶⁻⁸, mechanical reinforcement ^{9,10}, and ion conduction¹¹. The unique properties of PNCs depend on factors such as inorganic nanofiller type, dispersion, loading, as well as the polymer matrix characteristics. In most research, the fabrication of PNCs relies on mixing inorganic nanoparticles (NP) into a polymer matrix. Depending on processing conditions, the NPs can disperse by thermodynamic or kinetic trapping, or aggregate as NPs self-assemble to reduce unfavorable NP/matrix interactions. However, this general approach does not ensure a homogenous dispersion of NPs particularly when a high loading is required where initial interparticle spacing is on the length scale of the NP size. For instance, Krook et al (2019) investigated the miscibility of nanoplates in a lamellar diblock copolymer and found that the equilibrium interparticle spacing is 6.4 nm¹², implying limited and conditional miscibility of NP inside the polymer matrix. In another study by Krook et al (2018), when the concentration of monodisperse nanoplates increases to 0.05 vol% in the block copolymer (BCP) assembly, the nanoplates disrupt the lamellae structure of BCP resulting in a disordered system¹³. Thus, nanofiller dispersion in polymer matrices in most nanocomposites is limited to low loadings.

Preparing PNCs with a high loading of NPs is a challenge because most combinations of polymer and bare NPs result in aggregation of NPs. Though traditional PNCs typically contain low to moderate concentrations of inorganic nanofiller, for instance, commercial tires only

contain ~ 22 wt% carbon black nanofiller¹⁴, novel methods have been developed to increase NP loading. Lu et al (2003) performed free radical polymerization of monomers in the presence of NPs, thus trapping the NPs at a loading as high as 86 wt% (ca. 22 vol%) in the PNC¹⁵. Similarly, LaNasa and Hickey (2020) fabricated ultra-high loading PNCs by using a surface-induced ring-opening metathesis polymerization pathway to graft polymer chains on silica nanoparticles¹⁶. Srivastava and Kotov (2008) explored approaches to create PNCs with high loading through layer-by-layer assembly of polymers and NPs/nanowires¹⁷. Although these methods successfully produce PNCs with a high loading of NPs, there are some limitations to their applicability. Namely, the prior approach is limited to systems where the NP and monomer are miscible in a common solvent before initiating polymerization, whereas, the latter approach is limited to systems where the NP and polymer are oppositely charged.

To expand the possible combinations of polymer and NPs, a novel PNC method was developed using capillary rise infiltration (CaRI)¹⁸. This method starts with a two-layer system – a polymer thin film over a uniformly distributed layer of NPs. This bilayer was annealed above the polymer glass transition temperature (T_g) to fill the NP interstitial space via capillarity. Using nanoindentation and contact mode AFM, these PNCs were shown to exhibit a significant enhancement in scratch and wear resistance¹⁹, as well as high fracture toughness ^{20,21}. These PNCs also demonstrated increased hardness, modulus, and fracture toughness. Compared to other existing approaches for generating high NP loading PNC, CaRI is attractive because of its versatility, namely, compatibility with many NP fillers and polymer matrices, and ease of fabrication. However, in CaRI systems, the NP interstitial pore size is not uniform or homogeneous, and the random arrangement of NPs may result in colloidal level defects such as vacancies and interstitial particles. In this paper, we adapt CaRI to fabricate a new type of PNC

via infiltrating polymer into a nanoporous gold (NPG) exhibiting bicontinuous channels of gold and air. Limited research has been done utilizing NPG as a template for actuators and catalyst support^{22,23}. In our approach, polymer infiltrated nanoporous gold (PING) is presented as a new approach to achieve an interconnected polymer and metal structure that does not require a favorable thermodynamics of mixing. In a previous study, spectroscopic ellipsometry was shown to be a sensitive tool to characterize the thermal properties of fully infiltrated PNCs²⁴. In prior studies on the CaRI of polymers into nanoparticle films, polymer infiltration kinetics was also found to depend on polymer molecular weight, the extent of confinement, the presence of water and polymer-surface interactions ^{25–29}. We believe that the PNCs made by PING provides a simple and scalable platform to prepare membranes for actuators, gas separation and fuel cells.

The mechanism of polymer infiltration into nanoporous gold is capillary rise, a phenomenon where liquid spontaneously fills a narrow channel without the assistance of external forces. For Newtonian fluids, the capillary effect is described by the Lucas-Washburn Equation (LWE)^{30,31}.

$$h(t) = t^{0.5} \sqrt{\frac{R_{pore} Y \cos \theta_e}{2\eta_o}}$$
 Eq. 1

In Eq. 1, h(t) is the height infiltrated by the liquid, t is the infiltration time, R_{pore} is the radius of the pore, Υ is the surface tension of the liquid, θ_e is the equilibrium contact angle, and η_o is the fluid viscosity. The LWE assumes that the size of the fluid particle is an order of magnitude smaller than the radius of the channel, which enables the fluid to be treated as a continuum medium 30,32 . The scaling of polymer infiltration height h(t) with $t^{0.5}$ is well-documented. For example, polyethylene (PE) infiltrated into cylindrical anodized alumina oxide (AAO) nanopores exhibited LWE scaling such that flux $\sim t^{0.5}$, although the molecular weight dependence differed

from bulk behavior³³. Similar behavior was observed in molecular dynamics simulations of unentangled polymers in CaRI experiments³⁴. Polyethylene oxide (PEO) chains infiltrated into confined AAO cylindrical nanopores where $R_g \gg R_{pore}$ again exhibited LWE scaling $\sim t^{0.5~35}$. Interestingly, these studies found that low molecular weight PEO chains exhibited slower than theoretically predicted infiltration, whereas high molecular weight chains exhibited faster infiltration.

For these studies of capillary filling of PEO in nanopores, Yao et al. (2018) developed a model to account for these deviations from bulk viscosity scaling³²:

$$\frac{\eta_{eff}}{\eta_0} = \left[\left(\frac{R_{eff}}{R_{pore}} \right)^4 + \phi \frac{8N_e^{\square} b^3 \eta_0}{3NR_{pore}^2} \right]^{-1}$$
 Eq. 2

Here, the effective polymer viscosity, η_{eff} , deviates from the bulk viscosity, η_0 , due to two phenomena which dominate in distinct regimes of confinement. The first term in Equation 2 captures the dead zone effect, in which strong adsorption of chains to the capillary surface creates a zone of thickness ΔR where polymer imbibition is blocked. Accounting for this dead zone, the effective pore radius is defined as $R_{eff} = R_{pore} - \Delta R$. The reduced pore size increases η_{eff} , leading to infiltration dynamics slower than bulk behavior. The dead zone effect is expected to dominate when the polymer radius of gyration is much smaller than the pore radius, $R_g \ll R_{pore}$. Adapted from the work of Johner et al. (2010), the second term in Equation 2 describes reptation-like flow under confinement, which models infiltration as plug through a capillary³⁶. This term dominates in highly confined systems, i.e. when $R_g \gg R_{pore}$. Polymers confined in a reptation tube much smaller than their bulk length scale are driven by the capillary pressure gradient and infiltrate with a scaling of $\sim N^I$, showing enhanced mobility over bulk. In.

Eq. 2, ϕ is the fraction of chains participating in reptation, N_e is the entanglement length of the chains, b is the Kuhn length of the polymers, ζ is the friction coefficient of one Kuhn segment, and α is a general scaling exponent.

Deviations from the LWE have been observed both experimentally and computationally, with a variety of molecular weight scaling exponents ^{28,34,37,38}. Beyond the dead zone effect and modified reptation contributions enumerated in Equation 2, confinement can change other materials parameters that impact capillary rise infiltration of polymers in pores. For example, in contradiction to the PEO studies described previously ³⁵, experiments and self-consistent field theory simulations found that shorter chains can infiltrate *faster* than theoretically predicted³⁹. Such a contradiction demonstrates the complexity of polymer capillary rise infiltration and the other materials parameters that can impact the relationship in Equation 1.

The interaction between the infiltrating polymer and the scaffold surface is one such parameter. Diffusion of entangled polystyrene (PS) in a 2D slit geometry of alkylammonium modified mica-type silicates was found to scale inversely with molecular weight ($D \propto N^{-1}$) ⁴⁰. The weaker dependence than expected from reptation ($D \propto N^{-2}$) was attributed to attractive interactions between the polymer and confining surface. Using *in situ* nanodielectric spectroscopy, the infiltration kinetics of *cis*-1,4-polyisoprene (PI) in AAO nanopores proved quite different when the nanopores were silanized, a process which decreases PI-AAO adsorption⁴¹. Molecular dynamics simulations of polymer infiltrates into random close-packed NPs in the presence of solvent exhibited infiltration times with a non-monotonic dependence on polymer-NP interaction strength²⁸. Infiltration dynamics increases in speed as the polymer-NP attraction increases until a strong-adhesion limit is broached, beyond which infiltration slows.

The system in the present work, PS infiltration inside NPG, does not exhibit strong polymersurface attraction, existing well below this strong-adhesion limit.

The entanglement density of polymers is often cited as an explanation for the capillary infiltration dynamics of polymers. Using small angle x-ray scattering (SAXS) to follow PS infiltration into AAO cylindrical nanopores, an effective viscosity scaling of $\eta_{eff} \sim N^{1.5\pm0.1}$ was found for $R_g \gg R_{pore}$ and attributed to a confinement-induced reduction in entanglements during infiltration³⁷. Recent molecular dynamics simulations of polymer infiltration into a cylindrical nanopore measured a reduction in entanglements during capillary infiltration which scales inversely with capillary radius³⁸. These observations align with work studying noninfiltrating polymers under confinement. Experimental study of ultrathin PS films revealed a decrease in entanglement density with decreasing film thickness⁴². Simulations of entangled polymers under thin film confinement demonstrate that uniaxial compression of chains drives chain segregation, reducing the number of accessible interchain contacts and thus reducing entanglements ^{43,44}. Further computational studies extended this finding to cylindrical confinement ^{45,46} and tortuous networks with multiple confinement length scales⁴⁷. Entanglements are of particular interest in this work, in which entangled PS chains infiltrate into a NPG scaffold.

As exemplified by Equation 2, infiltration kinetics depends strongly on the degree of confinement. The confinement ratio, Γ , is defined as $\Gamma = R_g/R_{pore}$, where R_g is the radius of gyration of the polymer, and R_{pore} is the radius of the pore. Using CaRI, polydimethylsiloxane (PDMS) infiltration was investigated into a dense silica NP packing with a confinement ratio, Γ , varying from 0.6 to 1.5. This system exhibited a crossover in diffusive behavior at $\Gamma = 1$, with

 $D \propto N^{-1}$ for $\Gamma > 1$ and a scaling exponent between 0 and -1 for $\Gamma < 1^{25}$. PS infiltration into similar silica NP packings at much higher degrees of confinement, Γ varying from 2 to 15, exhibited viscosity scaling $\eta_{eff} \sim N^{0.8}$ ²⁶. Beyond the pore radius, the pore geometry is an important factor in infiltration kinetics. Work comparing the infiltration of PS into AAO with a tortuosity close to 1 versus infiltration into tortuous porous glass finds an inverse scaling of infiltration velocity with tortuosity⁴⁸.

The present study quantitatively measures the kinetics of entangled PS infiltration into NPG under moderately confined conditions where R_g is slightly less than the R_{pore} . The experimental confinement ratio Γ varies from 0.47 to 0.77. The infiltration time scales with PS molecular weight as $\tau_{80\%} \propto M_w^{1.30 \pm 0.20}$, straying from bulk viscosity scaling with $M_w^{3.4}$. Further, the PS viscosity extracted from infiltration studies is reduced by over an order of magnitude compared to the bulk. This study of a moderately confined polymer is an important contribution to the field because of the bicontinuous pore geometry with zero-mean curvature, compared to studies of concave cylindrical pores of AAO and convex pore of nanoparticle packings. The unique properties of this system drove us to use molecular dynamics simulations of polymer infiltration into NPG to illuminate experimental findings. Simulation results well agree with experimental scaling, $\tau_{infiltration} \propto N^{1.4}$. These simulations provide insights into the mechanism of infiltration by analyzing transient chain level behavior such as the fraction of chains adsorbed to the gold surface, entanglement density, and chain R_g during infiltration. These simulation properties and their implications on experimental polymer infiltration kinetics are expounded upon in this work.

Materials & Method

Samples. The polystyrene (PS) samples with different molecular weights were purchased and used as received. Important molecular characteristics and length scales are described in Table 1.

Table 1. Characteristics of PS and confinement parameter values

Sample Name	M _w (Da)	PDI	R_g (nm)	$\Gamma = R_g/R_{pore}$
PS-424k	424,000	1.06	17.8	0.47
PS-610k	609,500	1.06	21.4	0.57
PS-807k	806,815	1.03	24.6	0.66
PS-954k	954,000	1.06	26.7	0.71
PS-1031k	1,031,454	1.06	27.8	0.74
PS-1133k	1,115,960	1.02	28.9	0.77

The PS in these studies are entangled with weight average molecular weights ranging from 424 kDa to 1,116 kDa and have a low polydispersity (PDI), less than 1.06. The calculated radius of gyration (Rg) is given by $R_g = \sqrt{\frac{b^2 N}{6}}$. The Rg is calculated from the Kuhn length, b = 1.8 nm for PS, and the number of Kuhn segments, $N = \frac{M_W}{M_O}$, where the Kuhn monomer molar mass for PS is 720 Da⁴⁹. Solutions of PS and toluene are prepared using 2.4 wt.% of polymer. The PS solution is stirred overnight. Then, the solutions are spin coated onto silicon wafers (1 cm x 1 cm) at 4000 rpm for 1 minute. After that, the polymer films are annealed at 100°C in the Mettler heating stage (Mettler FP-82) under argon flow for 10 minutes to ensure a complete evaporation of the

solvent. The resulting polymer thicknesses range from 150-500 nm as measured by reflectometer (Filmetrics F3UV).

Nanoporous Gold (NPG) Fabrication. NPG is crucial in this study as it is used as the structure and template for measuring the polymer kinetics during the PING formation. NPG are prepared using a gold alloy anodic corrosion methodology⁵⁰. A Au-Ag (12 karat) foil with Au₃₅Ag₆₅ at %, is purchased and used as received. 15.8 M Nitric Acid is used to selectively etch Ag from the 12 karat composite. As the Au-Ag foil is immersed in nitric acid, HNO₃ first dissolves the less noble Ag atoms at the interface, leaving behind the Au rich layer. Subsequently, the Au atoms nucleate and grow Au-rich islands, which in turn exposes the underlying layer containing Ag. The Au islands eventually form the bicontinuous structure used in this study. The fabrication and structural characterization of the NPG has been previously studied ^{51–53}. Due to the high mobility of the gold atoms, the NPG scaffolds are annealed at 175°C for 3 h prior to forming a bilayer with PS. This pre-annealing step prevents structural changes in the NPG during polymer infiltration at 150°C ²⁴.

Bilayer Formation. This NPG scaffold is then deposited on a PS film. To form the NPG/PS bilayer, the pre-annealed NPG (1cm x 1cm) is floated onto a DI-H₂O surface. The suspended NPG is then lifted from underneath by a silicon wafer previously coated with a thin PS film. The bilayer is then dried on a hot plate at 60°C until water is completely evaporated from the sample surface.

In Situ Ellipsometry. Spectroscopic ellipsometry (SE) (J.A. Woollam, Alpha SE) is used to determine the infiltration extent of polymer in the NPG. The utilized wavelength range is 380-900nm. A Linkam THMSEL350V heating stage with a vacuum chamber is used for heating. The accuracy of the heating stage is 0.1°C with respect to the set temperature. The

heating rate is 30°C/min, and the sealed chamber ensures a continuous flow of N₂ to prevent polymer degradation. The samples are heated to 70°C and held at this temperature for 5 minutes to ensure equilibrium before ramping to 150°C. Subsequently, the temperature is heated at a rate of 30°C/min and then held at 150 °C to study infiltration. Because the bulk PS T_g is 100°C, temperatures higher than 100°C will induce polymer infiltration into NPG. As a result, the infiltration time refers to the time after when the heating plate reaches 100°C. The heating stage takes ca. 1.7 min to ramp from 100°C to 150°C. During infiltration, the temperature is stably held at 150°C. Effective Medium Approximation (EMA) Model with two material constitutes (see SI for further information) is used to capture the change in optical constants within the NPG composite as polymer fills the pores and approaches the top surface. The infiltration extent (IE) is given by, $IE = \frac{(n_t - n_i)}{(n_f - n_i)}$. The initial refractive index, n_i , is calculated by averaging the refraction index values during the first six min (i.e., prior to the PS infiltration). The final refractive index (after complete infiltration), n_f , is calculated by averaging the refraction index during the last two minutes when infiltration is complete. Details of the EMA fitting model are given in the SI.

Small Angle X-Ray Scattering (SAXS). Dual Source and Environmental X-Ray Scattering (DEXS, Xenocs Xeuss 2.0) at University of Pennsylvania is used for measuring NPG ligament-ligament distance. Six tubes with sample to detector distance of 6390 mm results in a q_0 range of 0.003-0.09 Å⁻¹. Cu K α , with a wavelength of 1.54 Å, is used as the light source. NPG samples are peeled off from the substrate using Kapton tape. The scattering data is collected for 1 h for each sample. The collected spectra are then azimuthally integrated into a curve for analysis. A control scattering collection of pure Kapton tape is also performed for 1 h to eliminate any effect from the tape on the scattering curve.

Water Contact Angle Goniometry. Static and Dynamic Water Contact Angles are used to measure the surface energy of the NPG/PS composite. Uniform DI-H₂O droplets were deposited onto the sample surface using a Gilmont Micrometer Dispenser. The system is illuminated using a Stocker Yale Imagelite Lite Mite - Model 20. Pictures of the water droplets were captured using a Sony CCD N50 Video Camera Module with a Navitar Zoom 7000 close-focusing macro video lens mounted on an optical table. The captured pictures are analyzed using Image J, plugin "LB-ADSA," which uses the Young-Laplace equation to fit the shape of the water droplet for the exact contact angle.

Atomic Force Microscopy (AFM). Bruker Icon AFM with tapping mode is used to probe the surface morphology of the NPG/composite. The images collected are $2*2 \mu m^2$. Tapping mode AFM tips, Tap300Al, have a tip height of 17 μ m and radius of 10 nm. The AFM images are analyzed using Gwyddion software.

Scanning Force Microscopy (SEM). FEI Quanta 600 SEM is used to detect the secondary electron signals at 15kV. The images are taken top-down to measure the ligament-ligament distance and in cross-section to measure the NPG thickness as well as infiltration extent. SEM images analysis also utilizes Gwyddion software.

Simulation Details. All simulations are performed on Stampede2 from the Texas Advanced Computing Center (TACC) through the Advanced Cyberinfrastructure Coordination Ecosystem: Services & Support (ACCESS) program⁵⁴ using LAMMPS with the Velocity Verlet algorithm and a Nose-Hoover thermostat⁵⁵ in the canonical (NVT) ensemble. Periodic boundary conditions are used in the x and y directions, with infiltration progressing in the z direction.

Entangled polymer melts are simulated using a modified coarse-grained bead-spring Kremer-Grest (KG) model ⁵⁶. Nonbonded monomers interact through the LJ potential $U_{ij}^{nb} = 4\epsilon \left[\left(\frac{\sigma}{r} \right)^{12} - \left(\frac{\sigma}{r} \right)^{6} \right] - 4\epsilon \left[\left(\frac{\sigma}{r_{cut}} \right)^{12} - \left(\frac{\sigma}{r_{cut}} \right)^{6} \right]$ for $r \leq r_{cut} = 2.5\sigma$. Units are non-dimensionalized using the potential strength, ϵ ; monomer size, σ ; and unit time, $\tau = \sigma \left(\frac{m}{\epsilon} \right)^{\frac{1}{2}}$, where m is the monomer mass. Monomers bonded together on the same chain interact via a finitely extensible nonlinear elastic (FENE) potential $U_{ij}^{b} = -0.5kR_{0}^{2} \ln \left[1 - \left(\frac{r}{R_{0}} \right)^{2} \right] + 4\epsilon \left[\left(\frac{\sigma}{r} \right)^{12} - \left(\frac{\sigma}{r} \right)^{6} \right] + \epsilon$ with $k = \frac{30\epsilon}{\sigma^{2}}$ and $R_{0} = 1.5\sigma$. The original KG model is modified by the additional of an angular harmonic potential $U_{ang} = \frac{K_{\theta}}{2} (\theta - \theta_{0})^{2}$ where $K_{\theta} = 10$ per radian is the interaction strength and $\theta_{0} = 120^{\circ}$ is the equilibrium bond angle. This potential increases the average number of entanglements per chain without requiring long chain lengths, giving an average number of monomers between entanglements of $< N_{e} > \approx 17.5^{57}$.

Polymer films are generated by random growth of polymers in a simulation box with walls on the top and bottom, followed by the application of soft potentials to push overlapped monomers apart. For efficient equilibration of entangled polymers, connectivity-altering Monte Carlo moves are used 58,59 . Films are equilibrated at high temperature, T=1.2, and a time step of $\Delta t=0.002\tau$. Equilibration proceeds until diffusive behavior of the center of mass mean squared displacement (MSD) is observed. The MSD is calculated with a moving time origin for improved statistics, and three independent film configurations are generated for each system. All polymers in this study are above the entanglement degree of polymerization. The number of monomers per chain are 25, 50, 100, 150, and 200, with N/N_e approximately equal to 1.5, 3.0, 6.0, 8.5, and 11.5, respectively. The entanglement statistics during the equilibration of chains are

included in Figure S7 of the Supporting Information. The polymer density is $0.85/\sigma^{-3}$. The films have dimensions $L_x = L_y = 100\sigma$, $L_z = 40\sigma$. The polymer films are placed on a 2σ thick support consisting of immobile LJ particles with a configuration taken from the middle 2σ of a larger film.

A simulation box with hard walls at the top and bottom and dimensions $L_x = L_y =$ 100σ , $L_z = 400\sigma$ is randomly filled with two types of LJ particles. A repulsive LJ potential is applied to induce spinodal decomposition. Simulations are run until the average ligament-toligament distance reaches the desired value, and then one of the two particle types is deleted, creating a nanoporous structure. LJ particles which are separated from the surface, or those with no nearest neighbors, are removed to create a nanoporous structure. The top and bottom surfaces are deleted, and the structure is placed $l\sigma$ from the top of the free surface of the supported polymer film. The LJ potential between particles within the nanoporous structure and polymer atoms is neutral i.e., $\epsilon = 1.0$ and $\sigma = 1.0$. Here, we create a nanoporous structure with an average pore radius $R_{pore}=6.27\sigma$. The structure factor of the nanoporous gold structure and characterization of the pore radius is included in Figure S8 of the Supporting Information. The confinement ratio is defined as the polymer radius of gyration within a bulk melt over the pore radius, $\Gamma = R_a/R_{pore}$. For the polymer lengths used in this work the confinement ratio ranges from $0.46 \le \Gamma \le 1.35$. The polymer is allowed to infiltrate the nanoporous structure during constant NVT dynamics at T = 1.2. The total number of LJ particles in our simulations is 1477795. Simulation images of the nanoporous gold structure, as well as initial and postinfiltration polymer configurations, are shown in Figure 1.

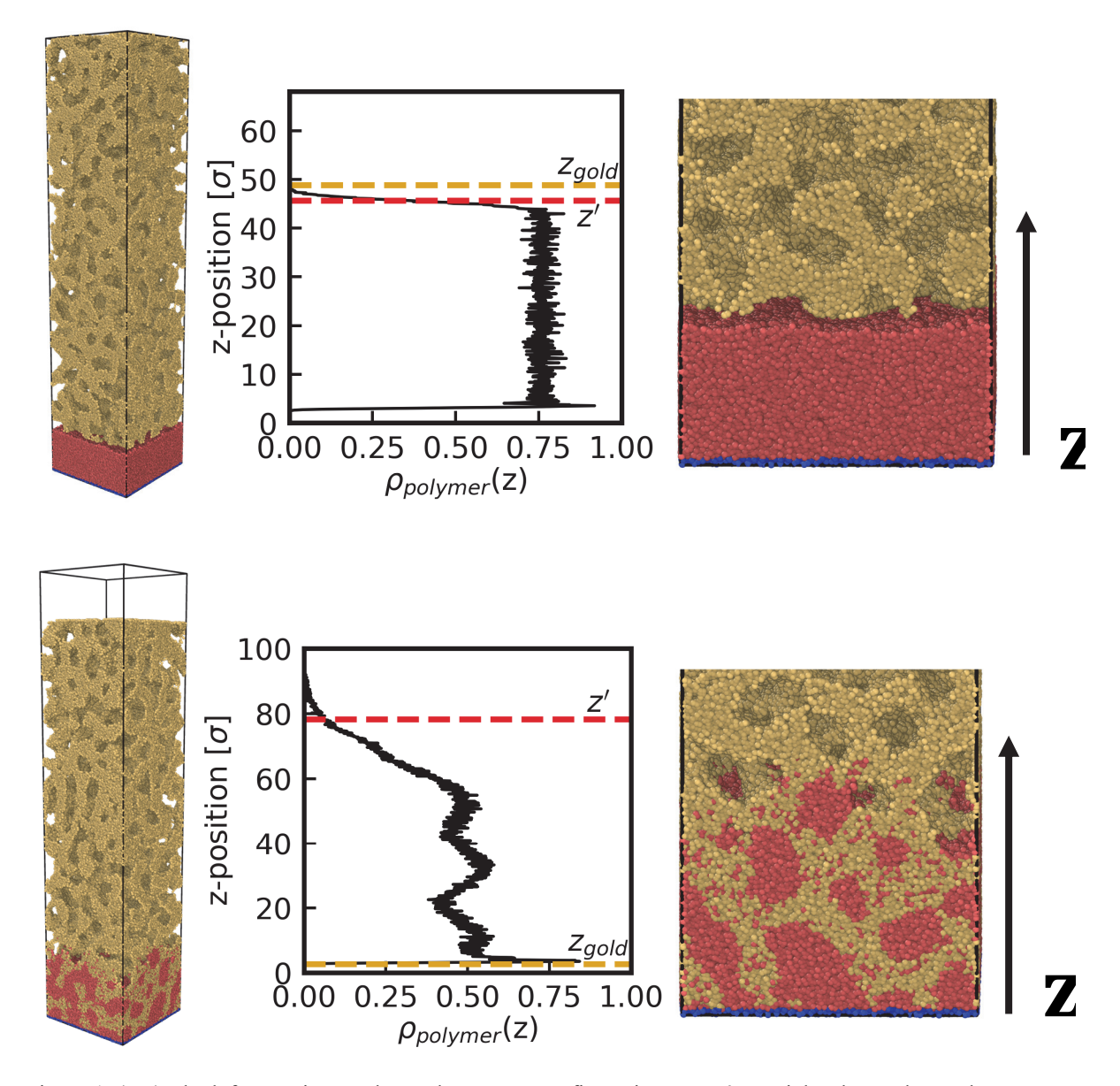


Figure 1. (top) The left-most image shows the system configuration at t=0. Particles that make up the nanoporous structure are shown in gold, polymer beads are shown in red, and particles within the thin support structure at the bottom of the polymer layer are shown in blue. The system is periodic in the x and y directions. The plot in the center shows the density profiles of polymer chains before infiltration versus z position for $\tau=0$. The right-most figure shows a zoomed in portion of the simulation box aligning with the density plot. (bottom) System configuration at t=165000000, or $\tau=330000$, showing polymer beads (red) partially infiltrating into nanoporous structure (gold). The plot shows the density profiles of polymer chains versus z position for $\tau=330000$. The right-most figure again shows a zoomed in portion of the simulation box aligning with the density plot. At this time point, all of the polymer reservoir has infiltrated into the nanoporous gold, and the gold structure has dropped to fill the empty space in the bottom of the simulation box. On both density plots, the dashed red horizontal line shows the z threshold z', where $\int_0^{z'} || \mathbf{r}| \rho(z) dz = 0.99 \rho_{total}$, or at which 99% of the total polymer density is contained. The dashed gold line shows the z position of the bottom of the nanoporous gold structure, z_{gold} . The polymer infiltration height, h_{99} , is defined as $z' - z_{gold}$.

Results and Discussion

Characterization of Nanoporous Gold (NPG).

In this study, polymer is infiltrated into the pores of a nanoporous gold (NPG) scaffold. The scaffold is prepared by dealloying a ca. 100 nm film with nominal composition Au₃₅Ag₆₅ at. %. In the gold-alloy etching process, also known as depletion gilding or gold coloration⁵⁰, the less-noble (Ag) element is removed, leaving behind Au adatoms that diffuse to form Au clusters and eventually Au ligaments. The resulting structure is bicontinuous with gold ligaments and nanopores as shown in Figure 2a. Figure 2a (inset) shows a cartoon of the NPG structure, that defines d which is the average distance from the center of one ligament to the center of an adjacent ligament. Because pristine NPG spontaneously coarsens at moderate temperature, post-dealloying coarsening is needed to stabilize the structure. Both thermal and chemical coarsening has been studied ^{51,53,60-62}. Because the NPG/PS infiltration studies utilize thermal annealing at 150°C (i.e. above the PS glass transition temperature), the NPG was thermally coarsened at 175°C for 3 h prior to preparing the NPG/PS bilayer. Our prior study showed that this treatment prevented NPG coarsening during infiltration at 150 °C ²⁴.

Small-angle X-ray scattering (SAXS), SEM and AFM were used to characterize the structure of the NPG. Figure 2b shows the SAXS intensity versus wavenumber (q) before and after coarsening the NPG at 175°C for 3 h. For as-prepared NPG, the maximum-intensity peak position is located at $0.00873 \, \text{Å}^{-1}$, corresponding to d = 89 nm, with a small shoulder at $0.02139 \, \text{Å}^{-1}$ which corresponds to d = 36 nm. This shoulder may reflect scattering from Au nanoparticles (NP) resulting from incomplete ligament formation. Upon annealing, the maximum intensity moves to lower q, $q_{\text{max}} = 0.00513 \, \text{Å}^{-1}$, and the shoulder disappears suggesting dissolution of the Au NP. For bicontinuous structures, the ligament-ligament distance

is given by $d=1.23*\frac{2\pi}{q_{max}}$ 51.63, where the factor of 1.23 accounts for the random arrangement of ligaments. For as prepared NPG, d is 89 nm, whereas after thermal treatment d=150 nm. The full width at half maximum (FWHM) of the annealed NPG is shown in SI Fig. S1. The broadness of the scattering peak reflects the heterogeneity of the pore size which is verified in SEM and AFM images. For annealed NPG, the lower bound of the FWHM is $q_{FWHM,lower}=0.00218~\mathring{A}^{-1}$, corresponding to $d_{upper}=355~nm$. The upper bound is $q_{FWHM,upper}=0.00829$ \mathring{A}^{-1} , corresponding to $d_{lower}=93~nm$. The calculation can be verified through the SEM/AFM images in Figure 2, as some pores have larger values in the longitudinal direction. As noted previously, this thermal treatment is sufficient to lock in the NPG structure during polymer melt infiltration at 150°C. For all subsequent discussion, "NPG" will refer to the coarsened structure.

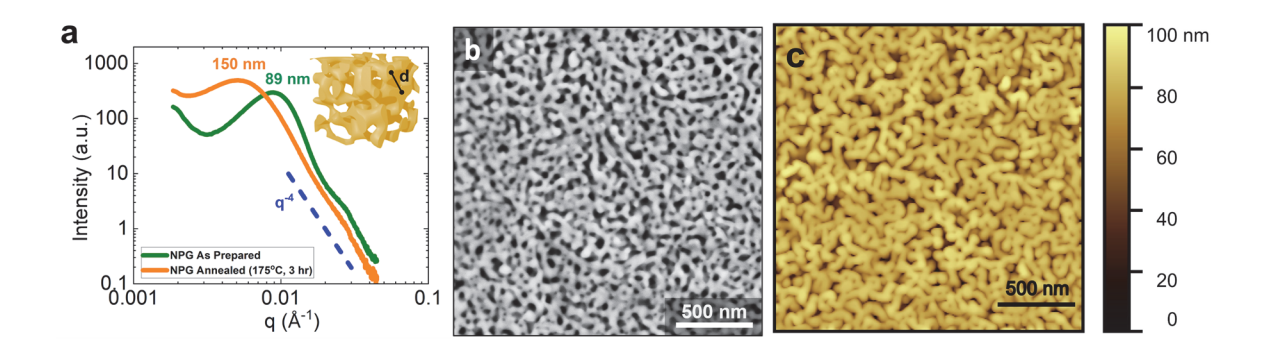


Figure 2. NPG structural analysis. A) SAXS spectra of as-prepared and coarsened (175°C, 3 h) NPG film. The maximum q values are used to determine d values of 89 nm and 150 nm, respectively. The high q region scales as q⁻¹. The inset defines d as the ligament to ligament spacing. Inset cartoon adopted from Welborn and Detsi (2020). B.) SEM and c) AFM height images of coarsened NPG in a top-view. White and gold colors, respectively, represent the ligaments of the NPG. Dark regions in both images correspond to open pores.

The coarsened NPG was also characterized by real space methods, namely SEM and AFM. Figure 2b is an SEM image showing that the NPG displays an interconnected network structure when viewed top down. Line-scans (see SI, Fig. S2) are used to determine the ligament-ligament distance, $d = 146 \pm 9$ nm, which is in good agreement with SAXS (Fig. 2a). Figure 2c is an AFM height image of the coarsened NPG exhibits a network of gold ligaments.

By taking a 2D correlation function, the ligament-ligament distance can be determined from the distance between peak heights as shown in SI (Fig. S3). To randomize measurements, correlations were determined at -45° , 0° , 45° , 90° . From AFM, the ligament spacing was found to be 114 ± 39 nm, which is less than the values from SAXS and SEM. The large uncertainty may result from limited resolution due to the tip radius (10 nm) as it traverses the narrow pores (75 nm). This resolution limit is evident upon comparing the narrower ligament widths in the SEM image (Fig. 2b) compared to the broader widths in the AFM height image (Fig. 2c).

Pore volume is another important characteristic of the NPG. In addition to d, the pore volume fraction and pore radius were determined for the NPG. As modeled via ellipsometry and calculated from 2D correlation function analysis of the AFM image (Fig. S3), the porosity of the NPG is approximately 50% by volume, which agrees well with our previous study²⁴. As shown in Fig. 2a, the ligament-ligament distance is the sum of the ligament width plus the diameter of the pore. Thus, the average radius of the pore is given by $R_{pore} = \frac{d}{4}$, which is 37.5 nm in this study.

Characterization of NPG/PS before and after complete infiltration.

Before investigating the kinetics of infiltration, the initial NPG/PS bilayer and the NPG/PS composite (PING) after complete infiltration were characterized. The preparation of NPG/PS on a silicon substrate was described in the Materials and Methods section. Figure 3a shows a cross-sectional SEM image of a bilayer with a 120 ± 4 nm thick NPG top layer (white) over a 80 ± 3 nm thick PS layer (dark). The edges of both films are observed as well as the gold ligaments on top of the NPG. Figure 3b presents a cross-section image of PS-424k in the NPG after complete infiltration at 150° C for 3 h. The final thickness of PING is 128 ± 8 nm. From

Figure 3, PS-424k appears to completely fill the pores. The NPG thickness before and after infiltration are within experimental uncertainty, indicating that the NPG takes up the PS without swelling.

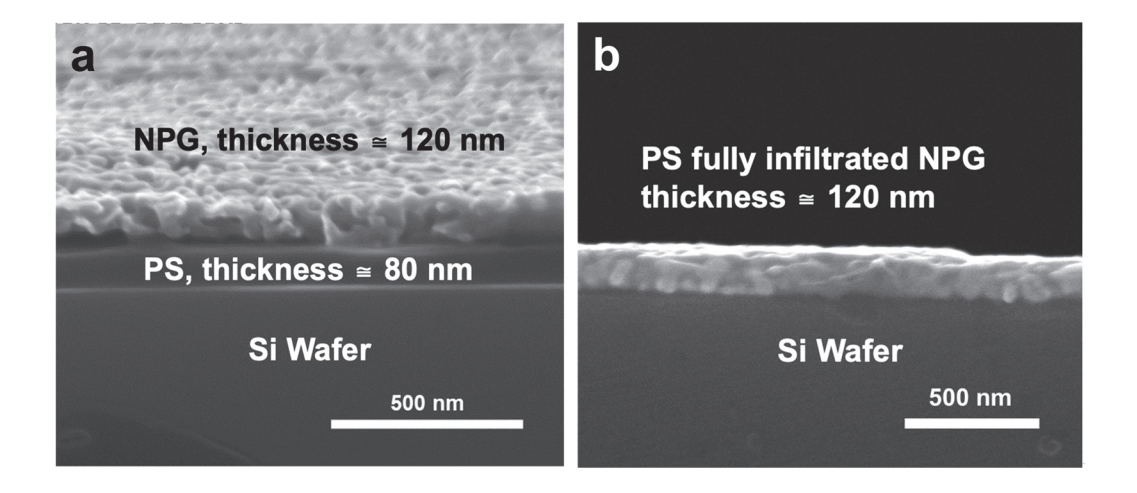


Figure 3. a) Cross-sectional SEM image of the prepared bilayer. The top-most, middle and bottom layers represent the NPG (120 nm), the PS film (80 nm), and the silicon substrate. The tilt angle is 5°. b) Cross-sectional SEM image of the NPG after complete infiltration by the PS-400k after annealing for 3 h at 150C.

The surface characteristics and properties of the fully infiltrated NPG/PS films were also determined. As polymer infiltrated the NPG from below, the color of the film became progressively dimmer as shown in Figure S4 as the film transitioned from initial to partial to complete infiltration. Tapping mode AFM was used to characterize the topography of the NPG/PS-424k film before and after complete infiltration as shown in Figure 4. The AFM tip radius is 10 nm. Before infiltration (t = 0 s), the NPG (\sim 120 nm) lies on top of the PS-424k film (\sim 80 nm) and, as expected, the height image in Fig. 4a is very similar to that in Fig. 2c for the neat NPG film. The bicontinuous gold ligament structure (bright features) can be clearly visualized. The height scale bar from 0 to 100 nm was chosen to be the same as that of Fig. 2d. The surface roughness of the bilayer is $R_q = 3.3 \pm 0.7$ nm, implying that the surface is relatively rough due to the open pores at the surface. However, after complete infiltration, Figure 4b

shows that the surface becomes smoother with ligaments (bright spots) rising at most ca. 50 nm above the background. This decrease in roughness is attributed to the PS domains (dark) filling the pores between ligaments. Quantitatively, the surface roughness decreases to $R_q = 1.8 \pm 0.1$ nm.

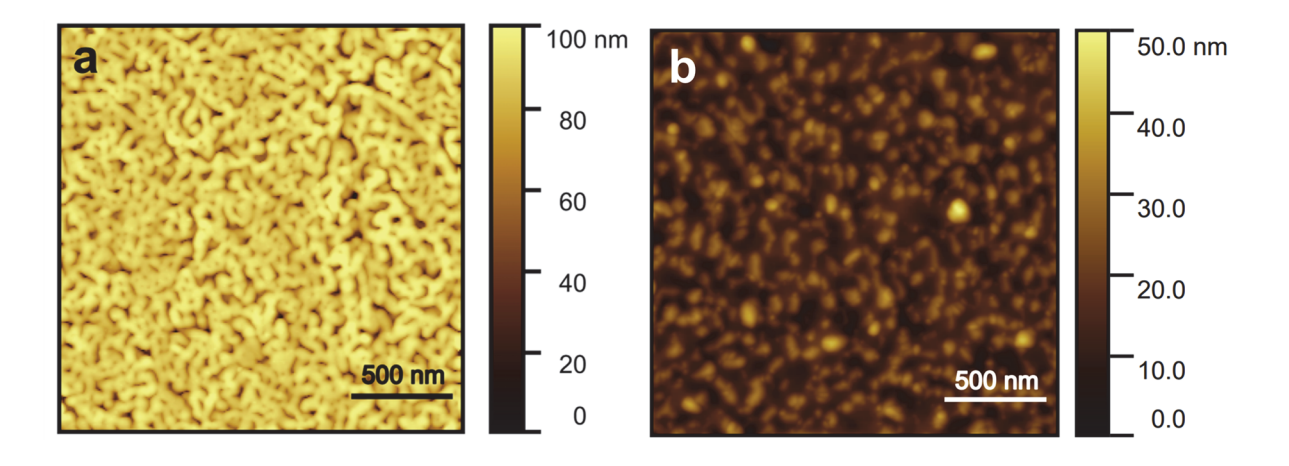


Figure 4. a) AFM height image of NPG (ca. 100 nm) over PS-424k film (ca. 100 nm). Surface roughness is $R_q = 3.3 \pm 0.7$ nm. The structure is similar to that in Figure 2c. b. AFM height image of the NPG after complete infiltration by PS-424k after annealing at 150°C for 3 h. Surface roughness is $R_q = 1.8 \pm 0.1$ nm

To further investigate surface properties, water contact angles were measured on a pure PS-954k film, a solid gold film and a fully infiltrated NPG/PS-954k film. As shown in Figure 5a, the equilibrium water contact angle for PS-900k is $\theta = 89.9 \pm 0.7^{\circ}$, in good agreement with literature⁶⁴. Because it is porous, the NPG absorbs water and delaminates from the substrate. Thus, a solid gold film was used as a surrogate for the NPG film. The gold wafer, made by sputtering a layer of gold on a silicon wafer, exhibits a water contact angle $\theta = 64.4 \pm 2.7^{\circ}$, which is in good agreement with the range of values from the literature, 60 to 65° ⁶⁵. Given that the porosity of the NPG is ca. 50%, the water contact angle for fully infiltrated NPG can be estimated by averaging the contact angles of PS-954k and gold, and is 77.2°. This estimate assumes a smooth surface and does not account for the effect of nanoscale roughness shown in

Fig. 4b. As shown in Figure 5, the measured contact angle for the NPG/PS-954k film is slightly larger, $\theta = 80.1 \pm 0.5^{\circ}$, than the simple rule of mixtures prediction. This small difference might be attributed to PS domains that partially spread over the gold ligaments on the top surface. Nevertheless, because $\theta < 90^{\circ}$, the top of the NPG/PS-954k film appears to contain both PS domains and gold ligaments at the surface. The water contact angle results are qualitatively consistent with the AFM height map shown in Figure 4b that displays patches of PS (dark) and gold ligaments (bright). Thus the AFM results suggest that PS does not spread across the entire surface to form a uniform wetting layer over the gold ligaments. AFM phase images shown in Figure S5 of the SI support this conclusion. In addition to the static contact angle, we have also measured the dynamic water contact angle on fully infiltrated NPG/PS-954k as shown in Fig. S6. Future studies will apply ToF-SIMS to quantify the relative areas of PS and gold on the surface.

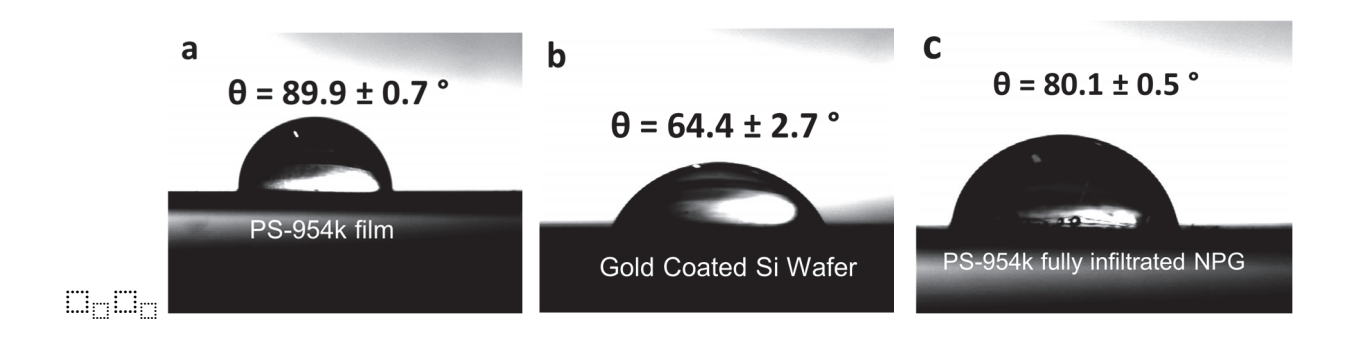


Figure 5. Room temperature water contact angle measurements on a) PS-954k film, b) solid gold film on silicon, and (c) NPG after complete infiltration by PS-954k.

Kinetics of Polystyrene Infiltration into the NPG Scaffold.

After characterizing the initial and final states, the kinetics of polystyrene infiltration into a NPG scaffold is investigated using *in-situ* spectroscopic ellipsometry (SE). The infiltration extent (IE) is determined from the refractive index of the top layer at time t, n_t , via $IE = \frac{(n_t - n_i)}{(n_f - n_i)}$, where n_i is the initial refraction index of the top layer, and n_f is the final refraction

index of the top layer (see SI for details). Figure 6 shows the IE as a function of annealing time for PS-954k infiltrating into NPG at 150°C. From 0 to 10 min, PS-954k fills approximately 35% of the NPG; however, from 10 to 20 min, PS-954k only fills an additional 23% of the NPG. The slower kinetics of PS infiltration is reflected by the parabolic shape with a negative concavity shown in Fig. 6b. According to the classical LWE model, the capillary driving force becomes weaker as infiltration increases resulting in a slowing down of the advancing polymer front. To compare infiltration times as a function of PS molecular weight, the time to infiltrate 80% of the NPG, $\tau_{80\%}$, was chosen. This time point was convenient for several reasons. First, the 80% filling fraction value can be more accurately measured than the 100% value which is approached asymptotically as shown in Figure 6b. Further, using $\tau_{80\%}$ allows for a higher molecular weight range to be explored using reasonable annealing times. Figures 6a and 6b show that $\tau_{80\%} = 38.8$ min for PS-954k infiltrating into the NPG at 150°C.

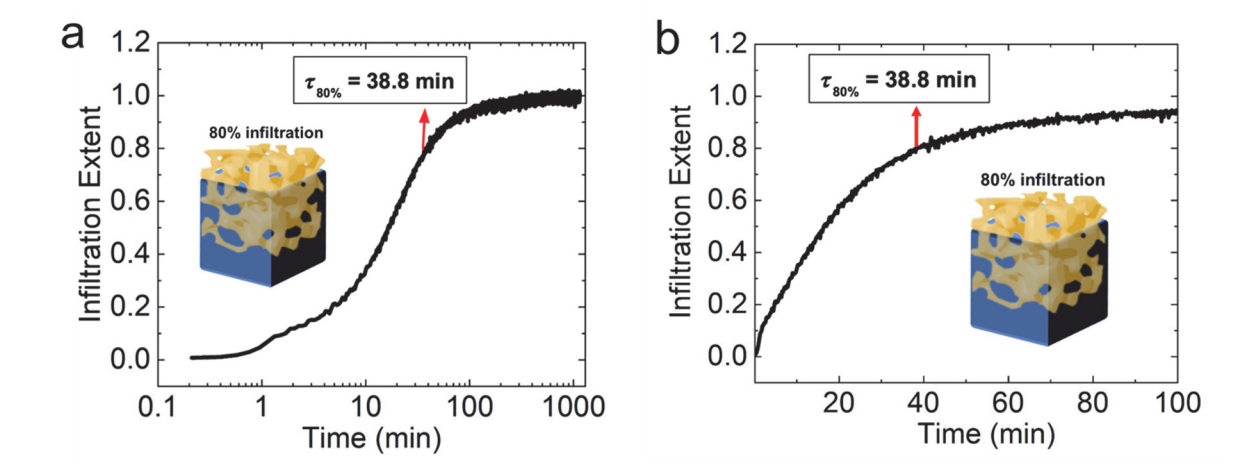


Figure 6. Infiltration of PS-954k into NPG at 150° C. (a) Plot of the infiltration extent as a function of the log time . (b). Plot of the infiltration extent as function of linear scale between t = 0 and t = 100 mins. The time to reach 80% infiltration is represented in the insets and has a value of 38.8 min for PS-954k at 150° C.

Using $\tau_{80\%}$ measurements from SE, the kinetics of polystyrene infiltration into NPG was measured for weight-average molecular weights (M_w) from 424k to 1133k g/mol. For a pore

radius of 37.5nm, the confinement ratio Γ ranges from 0.47 and 0.77 as shown in Table 1. Figure 7 shows how infiltration time increases as M_w increases upon annealing at 150°C. For example, PS-424k ($R_g=17.3$ nm) exhibits $\tau_{80\%}=9.69$ min, which is 5x faster than infiltration of PS-1133k ($R_g=28.9$ nm) where $\tau_{80\%}=49.9$ min. Note that the PS in this study (Table 1) have M_w values above the entanglement molecular weight of PS ($M_e=17$ k g/mol)⁴⁹ and therefore the bulk melt viscosity (η) scales as $\eta \propto M_w^{3.4}$ ^{49,66,67}. From the LW relationship, $\tau \sim \eta$, and therefore if bulk viscosity controls the molecular weight dependence of infiltration, $\tau_{80\%} \propto M_w^{3.4}$. However, as shown in Fig. 7, $\tau_{80\%} \propto M_w^{1.30\pm0.20}$, demonstrating that the molecular weight dependence of infiltration in NPG is much weaker than expected from bulk behavior.

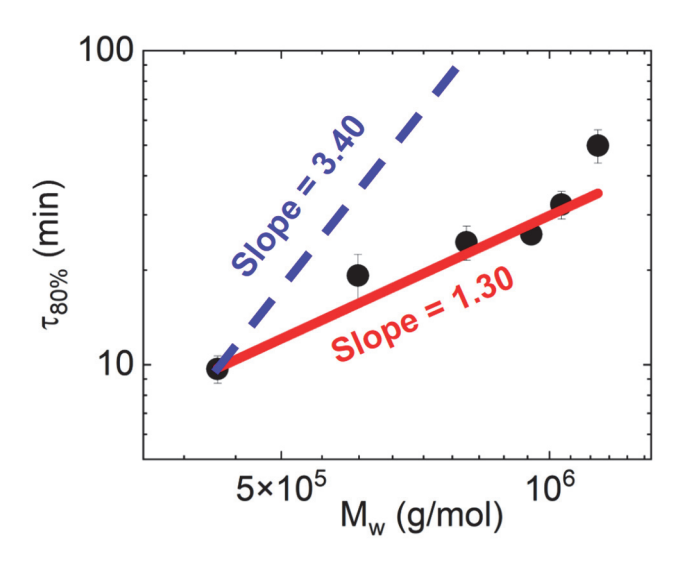


Figure 7. Infiltration time as a function of polystyrene molecular weight at 150°C. In these studies $\tau_{80\%}$ represents the time for PS to infiltrate 80% into the NPG scaffold. The scaling of $\tau_{80\%}$ with molecular weight is weaker than expected from bulk viscosity where $\tau_{80\%} \propto M_w^{3.4}$.

Next, we compare experimental results with prevailing models. For $R_g \gg R_{pore}$ and $\Gamma \gg 1$, Johner, Shin and Obukhov (2010) developed a theoretical model that captures reptation of

polymers under strong confinement. The pressure gradient within the pores results in enhanced mobility and faster infiltration³⁶ where $\tau \propto M_w^1$. In previous experiments under confinement 35,37 , the PS and PEO infiltration time in nano-sized cylindrical pores were found to scale as $\tau \propto M_w^{1.4}$ and $\tau \propto M_w^{0.9}$, respectively. Additionally, polymer infiltration in a densely packed SiO₂ nanoparticle scaffold scaled²⁶ as $\tau \propto M_w^{0.8}$. Though the polymers used in these studies were entangled, the scaling behavior approximately suggests that $\tau \propto \eta \propto M_w^1$. Thus, for both the model and experiments where $\Gamma > 1$, the infiltration rate exhibits a weaker dependence on M_w than expected from bulk behavior.

Infiltration time (Figure 7) can be used to determine the effective viscosity (η_{eff}) of PS. Using a modified Lucas-Washburn Equation (LWE) that accounts for tortuosity⁶⁸, the height that PS travels at time t is:

$$h^2 = \left(\frac{\Upsilon R_{pore} cos \theta}{4 \eta_{eff} \tau^2}\right) t$$
 Eq. 5

where Y is the surface tension of PS at 150°C, R_{pore} is the average pore which is 37.5 nm, τ is the tortuosity factor of the NPG ⁶⁹ which is taken as 1.5, θ is the contact angle between PS and gold ²⁶, which is assumed to be 20°. Calculations for the surface tension and bulk viscosity are given in the SI. As shown in Figure 8, the effective viscosity of PS infiltrating inside the NPG is lower than that of the bulk (η_{bulk}). For 424k-PS, η_{eff} is 7.0 * 10⁶ Pa*s and η_{bulk} is 2.9 * 10⁸ Pa*s, which is 40x greater than the viscosity of the confined polymer. For 1133k-PS, the reduction in viscosity is even larger with $\eta_{eff} = 3.8 * 10^7$ Pa*s and $\eta_{bulk} = 8.4 * 10^9$ Pa*s resulting in a difference of more than two orders of magnitude. As shown in Figure 8, the difference in $\eta_{bulk} - \eta_{eff}$ increases as M_w increases. As observed in MD simulations in Figure

10, one possible explanation is that the reduction in entanglement density increases as M_w increases. In summary, the PS infiltration time exhibits a weaker dependence on M_w than expected from bulk behavior and PS viscosity inside the nanopores is greatly reduced relative to bulk viscosity. In addition to predicting the scaling behavior of infiltration time with M_w , the next section will investigate the mechanism of infiltration using molecular dynamics simulations.

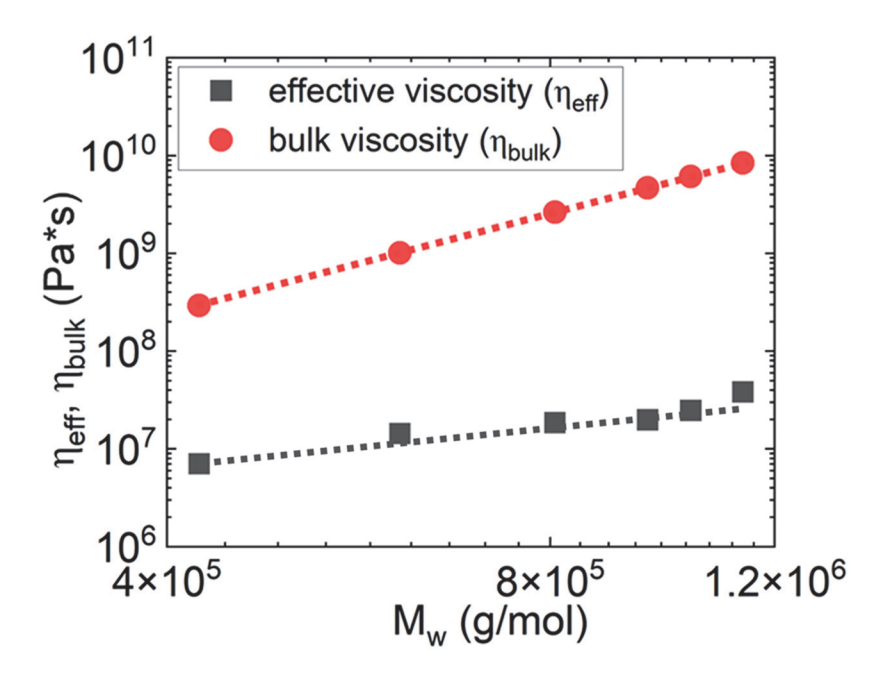


Figure 8. The effective viscosity of PS in the NPG and bulk viscosity as a function of molecular weight at 150°C. Red circles represent the bulk viscosity values calculated at the same molecular weight as the NPG studies. The dashed red line is a fit that scales as $M_w^{3.4}$. The gray squares represent the effective viscosity determined from the infiltration times given in Figure 7. The effective viscosities of PS confined in the NPG are much lower than the bulk values.

Molecular Dynamics (MD) Simulations of Polymer Infiltration into NPG.

To compare experimental results with simulations, molecular dynamics is used to determine the height of the polymer front as it infiltrates into the NPG. The methods section describes the system (Figure 1) and simulation details. The height of the polymer front is calculated from $\rho(z)$, the local polymer density in the z direction. The infiltration front can be

tracked as the z threshold z', where $\int_0^{z'} \square \rho(z) dz = 0.99 \rho_{total}$, or at which 99% of the total polymer density is contained. This threshold is depicted via a dashed red line in Figure 1 at $\tau = 0$ (initial configuration) and $\tau = 330000$ (after infiltration). The difference between this height and the bottom of the nanoporous gold structure, $z' - z_{gold}$, is referred to as $h_{99}(t)$. The infiltration rate, h_{99}^2 , is calculated from the slope of the linear region when plotting h^2_{99} versus time. To compare with experimental scaling of $\tau_{80\%}$ with molecular weight (Figure 7), $1/\dot{h}_{99}^2$, which is proportional to the infiltration time, $\tau_{infiltration}$, is plotted versus the number of monomers per chain N on a log-log plot. In previous works simulating polymer dynamics during capillary rise, in addition to tracking the infiltration front, the infiltration of the bulk of the polymer is characterized via the z threshold z'', where $\int_0^{z''} \square \rho(z) dz = 0.85 \rho_{total}$, or at which 85% of the total polymer density is contained³⁴. The dynamics of the infiltration front more closely match the experimental conditions tracked in this work and are thus reported here. The bulk infiltration dynamics are included in Figure S9 of the Supporting Information for completeness.

Figure 9 shows infiltration rate and infiltration time for N = 25, 50, 100, 150 and 200 monomers. Those five polymer chain lengths incorporate the range for PS used in the experiments, as N approximately ranges from 30 to 90 for the PS used in the experiments. Note that N/Ne increases from 1.5 to 11.5, respectively, for our simulated system. Figure 9a shows that the progression of infiltration slows down as polymer length increases. For each polymer, a linear regime is observed as expected from the LWE model. Figure 9b shows that infiltration time increases with N and that this time scales as $N^{1.4}$. This result is in good agreement with the experimentally observed scaling shown in Figure 7, where $\tau_{80\%} \propto M_W^{1.30 \pm 0.20}$. As discussed previously, this scaling deviates significantly from that expected for bulk behavior, $\tau_{80\%} \propto M_W^{3.4}$.

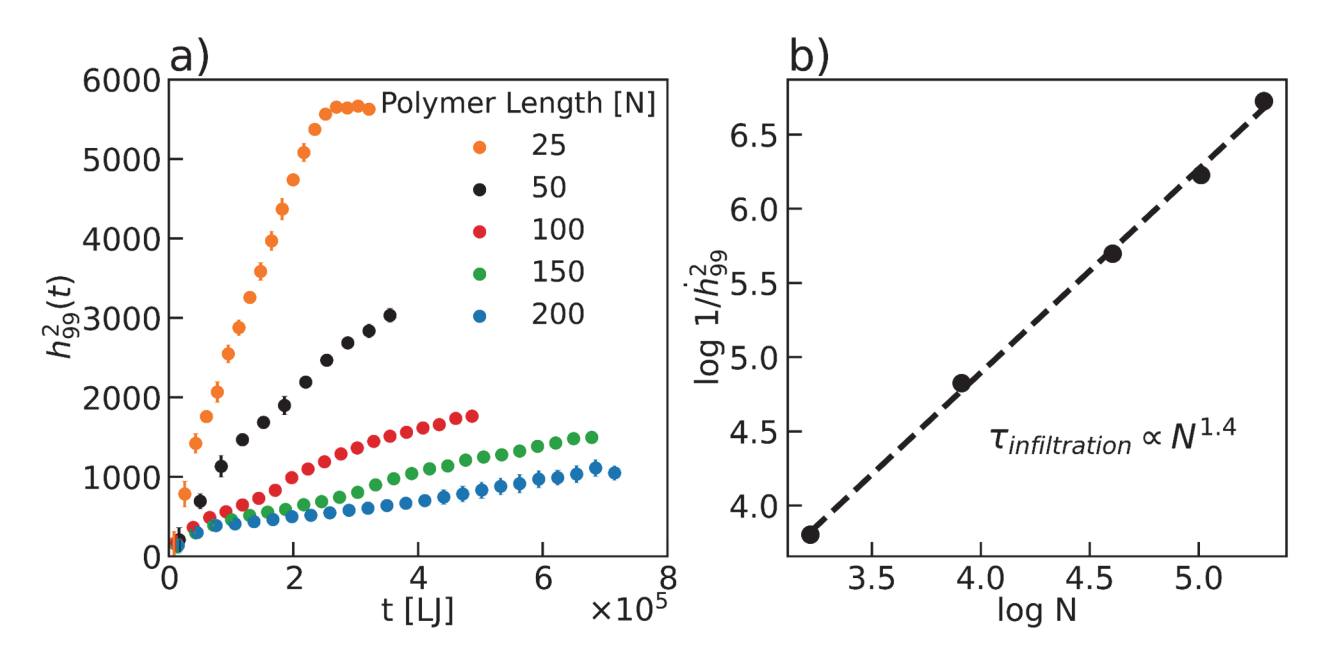


Figure 9. (a) The square of the infiltrated polymer film height h_{99}^2 as a function of simulation time. Each color corresponds to a different polymer chain length, N, as noted in the legend. An average of triplicate runs is shown, with error bars included on the plots. (b) Inverse infiltration rate $1/h_{99}^2$ as a function of the number of monomers. A log-log scale is used to show the scaling of infiltration time with N, $\tau_{infiltration} \propto N^{1.4}$.

The difference between the scaling from simulations and the $\tau \sim N^I$ behavior predicted by the model in Equation 2 may be attributed to several factors. The confinement ratio, Γ , in the simulations ranges from 0.46 to 1.35. The shorter chain lengths are not in the highly confined regime required for this reptation-like flow and lack sufficient entanglements to be considered within the reptation regime. In addition, the tortuosity of the gold surface changes the expected pressure gradient in comparison to an ideal cylindrical capillary³⁶.

Previous studies have shown that confinement reduces the number of entanglements in polymer chains compared to the bulk value 37,42,43,45,47 . A reduction in entanglements decreases polymer viscosity, thus leading to faster infiltration than predicted by bulk behavior. Figure 10a shows the change in the average number of entanglements per chain, $\Delta < Z >$, over the duration of infiltration for all chain lengths. Only infiltrated chains, i.e. chains with a center-of-mass z position above the bottom of the nanoporous gold structure, are considered for the average

number of entanglement analysis. The Z1+ algorithm⁷⁰ is used to analyze entanglements in all simulations. All chain lengths show a decrease in entanglements as infiltration time increases, consistent with the experimentally observed decrease in viscosity. As chain length and thus the degree of confinement increases, the magnitude of $\Delta < Z >$ increases from about -0.5 to -2.0 entanglements per chain for N = 25 and 250, respectively. Rather than using the loss of entanglements, comparing entanglement length, N_e , as chain length increases provides a clearer comparison. If the change in entanglements is sufficient to explain the confined polymer viscosity, one would expect $\eta \propto 1/N_e$, giving $\frac{\eta_{infiltrated}}{\eta_{bulk}} \propto \frac{Ne_{bulk}}{Ne_{infiltrated}}$. The ratio of bulk entanglement length versus infiltrated entanglement length during the course of infiltration is included in Figure S10 in the Supporting Information. Figure 10b shows $\frac{Ne_{bulk}}{Ne_{infiltrated}}$ versus Γ at the final simulation time point for each chain length, capturing the total change in the entanglement length over the course of infiltration. This ratio increases as N increases; if entanglements played a dominant role in the changes in the infiltration rate, we would thus expect smaller deviations from bulk viscosity for higher molecular weight polymers. However, with the dynamic scaling found experimentally and computationally in this work, $\frac{\eta_{infiltrated}}{\eta_{lm,lk}} \propto \frac{N^{1.4}}{N^{3.4}} \propto$ N^{-2} , one would expect larger deviations from bulk viscosity as N increases. The experimental results in Figure 8 show this latter trend; namely, the difference in $\eta_{bulk} - \eta_{eff}$ increases as M_w increases. Although a reduction in entanglements can enhance infiltration kinetics, the change in entanglement per chain does not explain the scaling observed in this study.

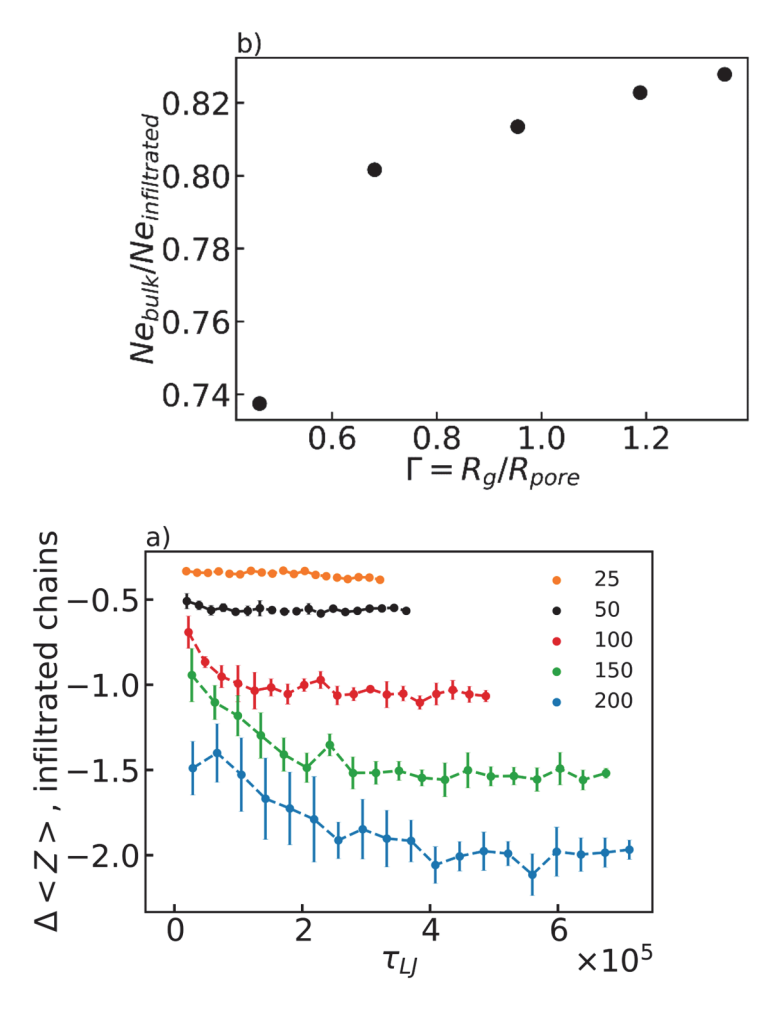


Figure 10. Effect of confinement on entanglements. (a) The decrease in the average number of entanglements per chain over the course of infiltration, $\Delta < Z > = < Z >_{t} - < Z >_{bulk}$. (b) $\frac{Ne_{bulk}}{Ne_{infiltrated}}$ at the final simulation time point versus the confinement ratio Γ .

The model from Yao et al (2018) assumes that chains obey Gaussian equilibrium statistics and are not deformed by flow^{32,36}. There have been conflicting results with regards to the shape of polymers during capillary infiltration, with reports of both unperturbed dimensions³⁷ and chain extension in the direction of flow³⁸. The reduction in entanglements for confined polymers is thought to be driven by chain compression in the confined dimension which reduces the pervaded volume of chains and thus the number of available interchain contacts ^{42,43}. Confinement of significantly long polymers can even drive chain segregation ^{44,46}. This chain segregation produces an entropic barrier to polymer diffusion, as chains must adopt highly

extended conformations to exchange positions with neighboring chains. Figure 11 shows the normalized one-dimensional radius of gyration in each direction for free (open circles) and highly adsorbed (solid circles) chains. Values are normalized to the bulk polymer Rg in each direction such that a value of 1 represents a chain that has retained bulk dimensions in that respective direction. Free chains are defined as those chains with no polymer beads within 1.5σ of any gold surface bead, while highly adsorbed chains have at least half of the total chain length within 1.5σ of any gold surface bead. There is clear extension in the direction of infiltration (z direction) for both free and adsorbed chains, with the extent of chain stretching scaling with the degree of confinement. Highly adsorbed chains retain bulk shape in the x and y directions for all confinement ratios, while the most confined free chains ($\Gamma = 1.35$) are compressed in the confined x and y directions.

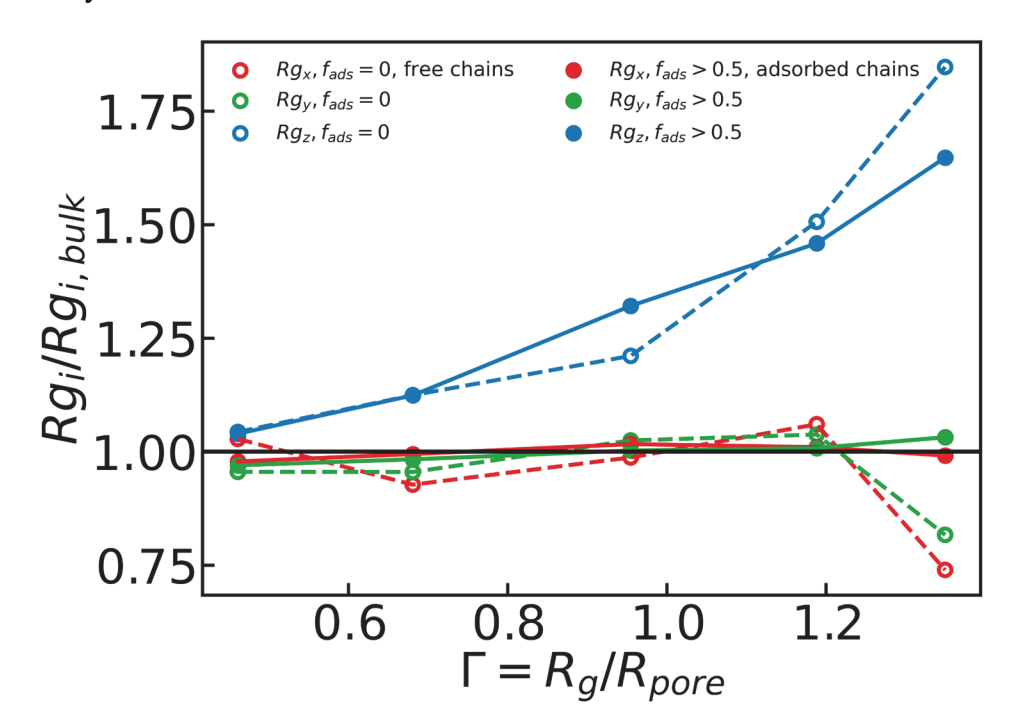


Figure 11. Normalized one-dimensional radius of gyration in each direction, split into free (open circles) and highly adsorbed (closed circles) chains. Free chains are defined as those with no polymer beads within 1.5σ of any gold surface bead, while highly adsorbed chains have at least half of the total chain length within 1.5σ of any gold surface bead. The x-axis corresponds to increasing chain length, plotted as the confinement ratio, R_g/R . Chain extension in the z-direction is observed for both free and adsorbed chains.

Although the dead zone effect is expected to slow infiltration compared to bulk behavior, the opposite effect to that observed in this system, we investigate if a dead zone could be present in simulations. To probe for a dead zone, we calculate $\frac{dz}{dt}$, the instantaneous velocity in the z direction of the center of mass of each polymer chain within the simulations. The effect of polymer surface adsorption on $\frac{dz}{dt}$ is quantified via the number of adsorbed beads out of the total number of beads of chain length N for each polymer. A bead is considered adsorbed if the chain bead is within 1.5σ of a gold surface bead. Figure 12a shows the z velocity dependence on the fraction of adsorbed beads per polymer, f_{ads} . The adsorbed fraction, f_{ads} , varies from 0 to 1 where $f_{ads} = 0$ represents a free chain not interacting with the gold surface and $f_{ads} = 1$ represents a chain fully adsorbed to the gold surface. For all chain lengths, the z velocity of the polymers decreases as the fraction of adsorbed beads increases. Despite this, even the longest chains exhibit motion at high f_{ads} , with $\frac{dz}{dt} > 0$. The lack of dead zone behavior is consistent with the experimental system because chains do not have a strong affinity for the gold surface, and thus are less likely to strongly and permanently adsorb to the surface.

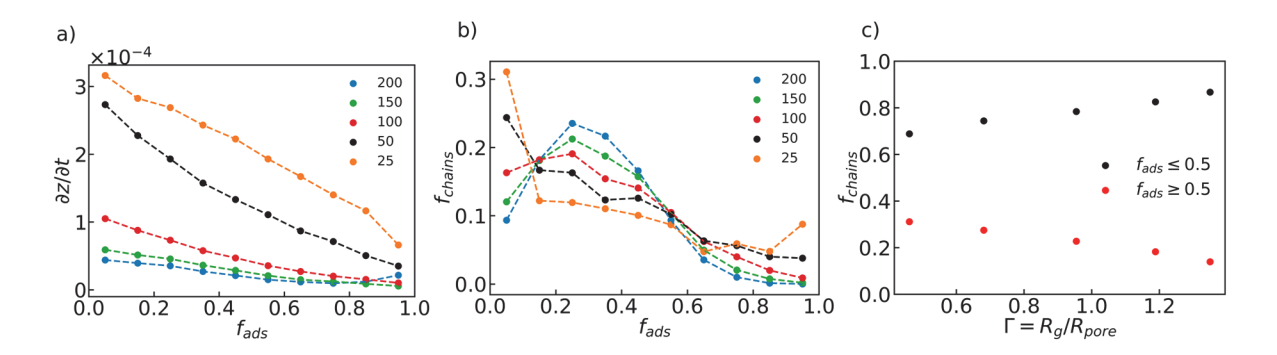


Figure 12. (a) Chain center of mass z velocity $\frac{dz}{dt}$, versus the fraction of adsorbed polymer beads for each chain length. A monomer is adsorbed if the chain bead is within 1.5σ of any gold surface bead. The adsorbed fraction is defined as $f_{ads} = (\frac{\# \ of \ adsorbed \ beads}{N})$. (b) The fraction of total chains (f_{chains}) at each adsorbed fraction for each

chain length. (c) The fraction of highly adsorbed chains $f_{ads} \ge 0.5$ (red) and the fraction of weakly adsorbed chains $f_{ads} \le 0.5$ (black) versus the confinement ratio Γ .

Figure 12b shows the fraction of total chains at each value of f_{ads} . This fraction is calculated using all time points throughout the course of infiltration. The two shortest chain lengths, N = 25 and N = 50, have radii of gyration smaller than the characteristic pore radius, Γ < 1. The highest fraction of chains for these polymers under low confinement are the free chains, with $f_{ads} < 0.1$. Once the radius of gyration is near or exceeds the pore radius, as is true for the other chain lengths (N=100, 150, 200), excluded volume interactions press chains toward the pore walls, and the largest fraction of chains exist in a partially adsorbed state.

In Figure 12b, above $f_{ads} \approx 0.6$, one sees that the number of chains with a large absorbed fraction decreases with increasing N. Despite the bias away from completely free chains, the fraction of slower moving, highly adsorbed chains is lower for longer chains. Figure 12c depicts this trend, plotting the fraction of highly adsorbed chains $f_{ads} \geq 0.5$ in red and the fraction of weakly adsorbed chains $f_{ads} \leq 0.5$ in black for each simulated Γ . This finding aligns well with previous works 39,71,72 demonstrating through both experiment and simulation that surface adsorbed polymer concentration scales inversely with molecular weight. A model for the probability distribution of adsorbed monomers has been developed previously 73 in which the mean value of f_{ads} is located at $f_{mean} \sim f_{max} - N^{-1/6}$ where f_{max} is the maximum adsorbed fraction. Such a model is for equilibrium distributions, which are not captured in Figure 12b, but demonstrates the N dependence of the adsorbed fraction. Previous research has also shown that polymer diffusion near surfaces exhibits non-monotonic behavior, at first increasing with increasing surface coverage until a maximum is reached and diffusion slows as macromolecular crowding at the surface dominates 74 . Combined with work demonstrating that shorter chain

lengths have faster adsorption dynamics³⁹, one would expect lower surface coverage with increasing N, as shown in Figure 12, and thus higher diffusion within the nanoporous gold in comparison with bulk diffusion.

Previous simulation work modeling the dynamics of polymers confined in nanoparticle packings found that polymer segments in contact with nanoparticle surfaces experienced higher local friction, and thus slower dynamics⁷⁵. When the authors compared a polymer nanocomposite system with a lower polymer fill fraction, $\phi_{\text{poly}} = 0.2$, to a system with higher polymer fill fraction, the higher $\phi_{\text{poly}} = 0.87$ system contained a notable number of chains with faster dynamics than the $\phi_{\text{poly}} = 0.2$ system. Since both systems have the same amount of available nanoparticle surface area, but there are more polymer chains in the more filled system, the polymers in the $\phi_{\text{poly}} = 0.2$ system have a higher percentage of polymer segments adsorbed to nanoparticle surfaces than the polymers in the $\phi_{poly} = 0.87$ system. The deviation in f_{ads} between the two systems leads to a difference in local friction, explaining the enhanced dynamics in the $\phi_{\text{poly}} = 0.87 \text{ system}^{75,76}$. A similar argument can be applied to the system studied here. As depicted in Figure 12, on average f_{ads} decreases with increasing chain length. The local friction due to surface adsorption in the system thus decreases with increasing chain length. The capillary force balance is between the pressure gradient and the frictional force. Under constant capillary pressure, the frictional force decreases with increasing chain length. One would thus expect larger deviations from bulk dynamics with increasing N due to a larger driving force during infiltration, which agrees well with the $\frac{\eta_{infiltrated}}{\eta_{bulk}} \propto \frac{N^{1.4}}{N^{3.4}} \propto N^{-2}$ experimental scaling behavior depicted in Figure 8, where the decrease from bulk viscosity grows with chain length.

The results from molecular dynamics simulations of capillary rise infiltration of weaklyinteracting entangled polymers into nanoporous gold reveal two main factors driving the experimentally observed reduction in viscosity and change in infiltration scaling exponent. The first is a reduction in chain entanglement density during infiltration. The number of entanglements decreases for all chain lengths studied, but there is a smaller delta in entanglements for larger chains. This trend means that entanglement density alone cannot fully explain the observed viscosity changes, where the decrease in viscosity increases with molecular weight. The second factor we attribute to the reduced viscosity is a decrease in the fraction of chains adsorbed with increasing polymer molecular weight. Less adsorption leads to decreasing friction with molecular weight, and thus lower viscosity.

Conclusion

In this work, the dynamic scaling of capillary rise infiltration of polystyrene as a function of molecular weight is measured inside a nanoporous gold (NPG) structure. The bicontinuous structure is characterized by SAXS, SEM and AFM. The NPG film is about 120 nm thick with a pore radius of 37.5 nm and a pore volume fraction of about 0.50. For a moderate degree of polymer confinement in the NPG (0.47 < Γ < 0.77) and entangled PS, the infiltration time scales as $\tau_{80\%} \propto M_W^{1.30\pm0.20}$, which is weaker than predicted if bulk viscosity dictates capillary flow. For $0.46 < \Gamma < 1.35$, molecular dynamics simulations of polymer infiltration inside NPG yields an apparent scaling $\tau_{infiltration} \propto N^{1.4}$, in good agreement with experimental studies. Using the infiltration time, the effective viscosity of entangled PS is significantly reduced compared to bulk, with the difference increasing with molecular weight. Molecular dynamics simulations of the nanoporous gold system demonstrate a reduction in entanglements for all chains, which supports the increased kinetics. However, the reduction in entanglements decreases as chain length increases, indicating that reduced entanglement alone does not explain the trend in

experimental viscosity. The simulations reveal a decrease in the fraction of highly adsorbed chains with N, which reduces polymer-wall friction with increasing polymer molecular weight. This behavior captures the observed experimental kinetics and viscosity. Through studying PS kinetics inside NPG during the formation of PING, we now better understand how to infiltrate polymers into a metal scaffold, facilitating future studies that utilize other polymeric materials to create PING that can serve as actuators, cell membranes, and optical response materials.

Associated Content

Author Information

Corresponding Authors

Russell J. Composto – Department of Materials Science and Engineering, University of Pennsylvania, Philadelphia, Pennsylvania 19104, United States.

Robert A. Riggleman – Department of Chemical and Biomolecular Engineering,
University of Pennsylvania, Philadelphia, Pennsylvania 19104, United States.

Daeyeon Lee – Department of Chemical and Biomolecular Engineering, University of Pennsylvania, Philadelphia, Pennsylvania 19104, United States.

Authors

Weiwei Kong – Department of Materials Science and Engineering, University of Pennsylvania, Philadelphia, Pennsylvania 19104, United States.

Anastasia Neuman – Department of Chemical and Biomolecular Engineering,
University of Pennsylvania, Philadelphia, Pennsylvania 19104, United States.

Aria C. Zhang – Department of Materials Science and Engineering, University of Pennsylvania, Philadelphia, Pennsylvania 19104, United States.

Author Contributions

R.J.C., D.L and R.A.R conceived and planned for the project. W.K. developed the experimental procedures and conducted all experimental measurements and analysis besides AFM measurements. A.N. conducted all simulation development and analysis. A.C.Z. took AFM

images. W.K and A.N. wrote the manuscript. R.J.C., D.L. and R.A.R edited the manuscript. All authors have given approval to the final version of the manuscript.

Acknowledgement

Experimental studies (WK, ACZ, RJC) were funded by the National Science

Foundation's (NSF) Division of Materials Research under grant DMR-1905912. Partial support
was received from ACS/PRF 62482-ND7 (WK, RJC) and the NSF NRT 2152205 (ACZ and
RJC). Simulation work (AN, RAR, DL) was supported by the NSF Process Systems, Reaction
Engineering, and Molecular Thermodynamics Program (CBET-1933704). WK acknowledges
support from the Vagelos Institute for Energy Science and Technology (VIEST) through the
2023-24 VIEST Fellowship. ACZ and AN received support from the NSF Graduate Research
Fellowship Program.

W.K. acknowledges Prof. Zahra Fakhraai (Penn, Chem) for helpful discussions on building experimental models. W.K. acknowledges Prof. Eric Detsi (Penn MSE) and Alexander Ng (Penn MSE) for helpful discussions in fabricating NPG and Prof. Karen Winey (Penn MSE/CBE) for helpful discussion on SAXS analysis. W.K. acknowledges the usage of Dual Source and Environmental X-ray Scattering (DEXS) facility operated by the Laboratory for Research on the Structure of Matter at the University of Pennsylvania (NSF MRSEC DMR-1720530). The DEXS equipment purchase was made possible by NSF MRI grant (17-25969), an ARO DURIP grant (W911NF17-1-0282), and the University of Pennsylvania. W.K. and A.C.Z also acknowledge characterization facilities in Singh Center for Nanotechnology, which is supported by the NSF Nanotechnology Coordinated Infrastructure Program under grant NNCI-2025608. Computational work used Stampede2 at the Texas Advanced Computing Center (TACC) through allocation MAT230002 from the Advanced Cyberinfrastructure Coordination

Ecosystem: Services & Support (ACCESS) program, which is supported by National Science Foundation grants #2138259, #2138286, #2138307, #2137603, and #2138296.

References

- (1) Balazs, A. C.; Emrick, T.; Russell, T. P. Nanoparticle Polymer Composites: Where Two Small Worlds Meet. *Science* **2006**, *314* (5802), 1107–1110. https://doi.org/10.1126/science.1130557.
- (2) Kim, J.; Park, E.; Moon, H.; Son, H.; Hong, J.; Wi, E.; Kwon, J.-T.; Seo, D. Y.; Lee, H.; Kim, Y. Estimation of the Concentration of Nano-Carbon Black in Tire-Wear Particles Using Emission Factors of PM10, PM2.5, and Black Carbon. *Chemosphere* **2022**, *303*, 134976. https://doi.org/10.1016/j.chemosphere.2022.134976.
- (3) Guth, E. Theory of Filler Reinforcement. *J. Appl. Phys.* **1945**, *16* (1), 20–25. https://doi.org/10.1063/1.1707495.
- (4) Bilchak, C. R.; Buenning, E.; Asai, M.; Zhang, K.; Durning, C. J.; Kumar, S. K.; Huang, Y.; Benicewicz, B. C.; Gidley, D. W.; Cheng, S.; Sokolov, A. P.; Minelli, M.; Doghieri, F. Polymer-Grafted Nanoparticle Membranes with Controllable Free Volume. *Macromolecules* **2017**, *50* (18), 7111–7120. https://doi.org/10.1021/acs.macromol.7b01428.
- (5) Merkel, T. C.; Freeman, B. D.; Spontak, R. J.; He, Z.; Pinnau, I.; Meakin, P.; Hill, A. J. Ultrapermeable, Reverse-Selective Nanocomposite Membranes. *Science* **2002**, *296* (5567), 519–522. https://doi.org/10.1126/science.1069580.
- (6) Glor, E. C.; Ferrier, R. C.; Li, C.; Composto, R. J.; Fakhraai, Z. Out-of-Plane Orientation Alignment and Reorientation Dynamics of Gold Nanorods in Polymer Nanocomposite Films. *Soft Matter* **2017**, *13* (11), 2207–2215. https://doi.org/10.1039/C6SM02403C.
- (7) Hore, M. J. A.; Frischknecht, A. L.; Composto, R. J. Nanorod Assemblies in Polymer Films and Their Dispersion-Dependent Optical Properties. *ACS Macro Lett.* **2012**, *1* (1), 115–121. https://doi.org/10.1021/mz200031g.
- (8) Hore, M. J. A.; Composto, R. J. Nanorod Self-Assembly for Tuning Optical Absorption. *ACS Nano* **2010**, *4* (11), 6941–6949. https://doi.org/10.1021/nn101725j.
- (9) Bilchak, C. R.; Huang, Y.; Benicewicz, B. C.; Durning, C. J.; Kumar, S. K. High-Frequency Mechanical Behavior of Pure Polymer-Grafted Nanoparticle Constructs. *ACS Macro Lett.* **2019**, *8* (3), 294–298. https://doi.org/10.1021/acsmacrolett.8b00981.
- (10) Rittigstein, P.; Torkelson, J. M. Polymer-Nanoparticle Interfacial Interactions in Polymer Nanocomposites: Confinement Effects on Glass Transition Temperature and Suppression of Physical Aging: Polymer-Nanoparticle Interfacial Interactions. *J. Polym. Sci. Part B Polym. Phys.* **2006**, *44* (20), 2935–2943. https://doi.org/10.1002/polb.20925.
- (11) Polizos, G.; Tuncer, E.; Agapov, A. L.; Stevens, D.; Sokolov, A. P.; Kidder, M. K.; Jacobs, J. D.; Koerner, H.; Vaia, R. A.; More, K. L.; Sauers, I. Effect of Polymer–Nanoparticle Interactions on the Glass Transition Dynamics and the Conductivity Mechanism in Polyurethane Titanium Dioxide Nanocomposites. *Polymer* **2012**, *53* (2), 595–603. https://doi.org/10.1016/j.polymer.2011.11.050.
- (12) Krook, N. M.; Tabedzki, C.; Elbert, K. C.; Yager, K. G.; Murray, C. B.; Riggleman, R. A.; Composto, R. J. Experiments and Simulations Probing Local Domain Bulge and String Assembly of Aligned Nanoplates in a Lamellar Diblock Copolymer. *Macromolecules* **2019**, *52* (22), 8989–8999. https://doi.org/10.1021/acs.macromol.9b01324.
- (13) Krook, N. M.; Ford, J.; Maréchal, M.; Rannou, P.; Meth, J. S.; Murray, C. B.; Composto, R. J. Alignment of Nanoplates in Lamellar Diblock Copolymer Domains and the Effect of Particle Volume Fraction on Phase Behavior. *ACS Macro Lett.* **2018**, 7 (12), 1400–1407. https://doi.org/10.1021/acsmacrolett.8b00665.
- (14) Gómez-Hernández, R.; Panecatl-Bernal, Y.; Méndez-Rojas, M. Á. High Yield and Simple One-Step Production of Carbon Black Nanoparticles from Waste Tires. *Heliyon* **2019**, *5*

- (7), e02139. https://doi.org/10.1016/j.heliyon.2019.e02139.
- (15) Lü, C.; Cui, Z.; Wang, Y.; Li, Z.; Guan, C.; Yang, B.; Shen, J. Preparation and Characterization of ZnS–Polymer Nanocomposite Films with High Refractive Index. *J Mater Chem* **2003**, *13* (9), 2189–2195. https://doi.org/10.1039/B304154A.
- (16) LaNasa, J. A.; Hickey, R. J. Surface-Initiated Ring-Opening Metathesis Polymerization: A Method for Synthesizing Polymer-Functionalized Nanoparticles Exhibiting Semicrystalline Properties and Diverse Macromolecular Architectures. *Macromolecules* 2020, 53 (19), 8216–8232. https://doi.org/10.1021/acs.macromol.0c01381.
- (17) Srivastava, S.; Kotov, N. A. Composite Layer-by-Layer (LBL) Assembly with Inorganic Nanoparticles and Nanowires. *Acc. Chem. Res.* **2008**, *41* (12), 1831–1841. https://doi.org/10.1021/ar8001377.
- (18) Huang, Y.-R.; Jiang, Y.; Hor, J. L.; Gupta, R.; Zhang, L.; Stebe, K. J.; Feng, G.; Turner, K. T.; Lee, D. Polymer Nanocomposite Films with Extremely High Nanoparticle Loadings via Capillary Rise Infiltration (CaRI). *Nanoscale* **2015**, *7* (2), 798–805. https://doi.org/10.1039/C4NR05464D.
- (19) Jiang, Y.; Hor, J. L.; Lee, D.; Turner, K. T. Toughening Nanoparticle Films via Polymer Infiltration and Confinement. *ACS Appl. Mater. Interfaces* **2018**, *10* (50), 44011–44017. https://doi.org/10.1021/acsami.8b15027.
- (20) Qiang, Y.; Turner, K. T.; Lee, D. Role of Polymer–Nanoparticle Interactions on the Fracture Toughness of Polymer-Infiltrated Nanoparticle Films. *Macromolecules* **2023**, *56* (1), 122–135. https://doi.org/10.1021/acs.macromol.2c01567.
- (21) Qiang, Y.; Pande, S. S.; Lee, D.; Turner, K. T. The Interplay of Polymer Bridging and Entanglement in Toughening Polymer-Infiltrated Nanoparticle Films. *ACS Nano* **2022**, *16* (4), 6372–6381. https://doi.org/10.1021/acsnano.2c00471.
- (22) Biener, J.; Biener, M. M.; Madix, R. J.; Friend, C. M. Nanoporous Gold: Understanding the Origin of the Reactivity of a 21st Century Catalyst Made by Pre-Columbian Technology. *ACS Catal.* **2015**, *5* (11), 6263–6270. https://doi.org/10.1021/acscatal.5b01586.
- (23) Li, J.; Markmann, J.; Weissmüller, J.; Mameka, N. Nanoporous Gold-Polypyrrole Hybrid Electrochemical Actuators with Tunable Elasticity. *Acta Mater.* **2021**, *212*, 116852. https://doi.org/10.1016/j.actamat.2021.116852.
- (24) Maguire, S. M.; Bilchak, C. R.; Corsi, J. S.; Welborn, S. S.; Tsaggaris, T.; Ford, J.; Detsi, E.; Fakhraai, Z.; Composto, R. J. Effect of Nanoscale Confinement on Polymer-Infiltrated Scaffold Metal Composites. *ACS Appl. Mater. Interfaces* **2021**, *13* (37), 44893–44903. https://doi.org/10.1021/acsami.1c12491.
- (25) Venkatesh, R. B.; Lee, D. Interfacial Friction Controls the Motion of Confined Polymers in the Pores of Nanoparticle Packings. *Macromolecules* **2022**, *55* (19), 8659–8667. https://doi.org/10.1021/acs.macromol.2c01282.
- (26) Venkatesh, R. B.; Lee, D. Conflicting Effects of Extreme Nanoconfinement on the Translational and Segmental Motion of Entangled Polymers. *Macromolecules* **2022**, *55* (11), 4492–4501. https://doi.org/10.1021/acs.macromol.2c00145.
- (27) Hor, J. L.; Wang, H.; Fakhraai, Z.; Lee, D. Effect of Physical Nanoconfinement on the Viscosity of Unentangled Polymers during Capillary Rise Infiltration. *Macromolecules* **2018**, *51* (14), 5069–5078. https://doi.org/10.1021/acs.macromol.8b00966.
- (28) Venkatesh, R. B.; Zhang, T.; Manohar, N.; Stebe, K. J.; Riggleman, R. A.; Lee, D. Effect of Polymer–Nanoparticle Interactions on Solvent-Driven Infiltration of Polymer (SIP) into Nanoparticle Packings: A Molecular Dynamics Study. *Mol. Syst. Des. Eng.* **2020**, *5* (3), 666–674. https://doi.org/10.1039/C9ME00148D.
- (29) Hor, J. L.; Wang, H.; Fakhraai, Z.; Lee, D. Effects of Polymer–Nanoparticle Interactions on the Viscosity of Unentangled Polymers under Extreme Nanoconfinement during Capillary Rise Infiltration. *Soft Matter* **2018**, *14* (13), 2438–2446. https://doi.org/10.1039/C7SM02465G.

- (30) Washburn, E. W. The Dynamics of Capillary Flow. *Phys. Rev.* **1921**, *17* (3), 273–283. https://doi.org/10.1103/PhysRev.17.273.
- (31) Lucas, R. Ueber das Zeitgesetz des kapillaren Aufstiegs von Flüssigkeiten. *Kolloid-Z.* **1918**, 23 (1), 15–22. https://doi.org/10.1007/BF01461107.
- (32) Yao, Y.; Butt, H.-J.; Floudas, G.; Zhou, J.; Doi, M. Theory on Capillary Filling of Polymer Melts in Nanopores. *Macromol. Rapid Commun.* **2018**, *39* (14), 1800087. https://doi.org/10.1002/marc.201800087.
- (33) Hu, G.; Cao, B. Flows of Polymer Melts through Nanopores: Experiments and Modelling. *J. Therm. Sci. Technol.* **2013**, *8* (2), 363–369. https://doi.org/10.1299/jtst.8.363.
- (34) Shavit, A.; Riggleman, R. A. The Dynamics of Unentangled Polymers during Capillary Rise Infiltration into a Nanoparticle Packing. *Soft Matter* **2015**, *11* (42), 8285–8295. https://doi.org/10.1039/C5SM01866H.
- (35) Yao, Y.; Alexandris, S.; Henrich, F.; Auernhammer, G.; Steinhart, M.; Butt, H.-J.; Floudas, G. Complex Dynamics of Capillary Imbibition of Poly(Ethylene Oxide) Melts in Nanoporous Alumina. *J. Chem. Phys.* **2017**, *146* (20), 203320. https://doi.org/10.1063/1.4978298.
- (36) Johner, A.; Shin, K.; Obukhov, S. Nanofluidity of a Polymer Melt: Breakdown of Poiseuille's Flow Model. *EPL Europhys. Lett.* **2010**, *91* (3), 38002. https://doi.org/10.1209/0295-5075/91/38002.
- (37) Shin, K.; Obukhov, S.; Chen, J.-T.; Huh, J.; Hwang, Y.; Mok, S.; Dobriyal, P.; Thiyagarajan, P.; Russell, T. P. Enhanced Mobility of Confined Polymers. *Nat. Mater.* **2007**, *6* (12), 961–965. https://doi.org/10.1038/nmat2031.
- (38) Zhang, J.; Lei, J.; Tian, W.; Zhang, G.; Floudas, G.; Zhou, J. Capillary Filling of Polymer Chains in Nanopores. *Macromolecules* **2023**, *56* (6), 2258–2267. https://doi.org/10.1021/acs.macromol.2c02157.
- (39) Yao, Y.; Butt, H.-J.; Zhou, J.; Doi, M.; Floudas, G. Capillary Imbibition of Polymer Mixtures in Nanopores. *Macromolecules* **2018**, *51* (8), 3059–3065. https://doi.org/10.1021/acs.macromol.7b02724.
- (40) Manias, E.; Chen, H.; Krishnamoorti, R.; Genzer, J.; Kramer, E. J.; Giannelis, E. P. Intercalation Kinetics of Long Polymers in 2 Nm Confinements. *Macromolecules* **2000**, 33 (21), 7955–7966. https://doi.org/10.1021/ma0009552.
- (41) Tu, C.-H.; Zhou, J.; Doi, M.; Butt, H.-J.; Floudas, G. Interfacial Interactions During In Situ Polymer Imbibition in Nanopores. *Phys. Rev. Lett.* **2020**, *125* (12), 127802. https://doi.org/10.1103/PhysRevLett.125.127802.
- (42) Wang, F.; Jiang, Z.; Lin, X.; Zhang, C.; Tanaka, K.; Zuo, B.; Zhang, W.; Wang, X. Suppressed Chain Entanglement Induced by Thickness of Ultrathin Polystyrene Films. *Macromolecules* **2021**, *54* (8), 3735–3743. https://doi.org/10.1021/acs.macromol.1c00224.
- (43) García, N. A.; Barrat, J.-L. Entanglement Reduction Induced by Geometrical Confinement in Polymer Thin Films. *Macromolecules* **2018**, *51* (23), 9850–9860. https://doi.org/10.1021/acs.macromol.8b01884.
- (44) Lee, N.-K.; Diddens, D.; Meyer, H.; Johner, A. Local Chain Segregation and Entanglements in a Confined Polymer Melt. *Phys. Rev. Lett.* **2017**, *118* (6), 067802. https://doi.org/10.1103/PhysRevLett.118.067802.
- (45) Sussman, D. M.; Tung, W.-S.; Winey, K. I.; Schweizer, K. S.; Riggleman, R. A. Entanglement Reduction and Anisotropic Chain and Primitive Path Conformations in Polymer Melts under Thin Film and Cylindrical Confinement. *Macromolecules* **2014**, *47* (18), 6462–6472. https://doi.org/10.1021/ma501193f.
- (46) Pressly, J. F.; Riggleman, R. A.; Winey, K. I. Polymer Diffusion Is Fastest at Intermediate Levels of Cylindrical Confinement. *Macromolecules* **2018**, *51* (23), 9789–9797. https://doi.org/10.1021/acs.macromol.8b01728.
- (47) Zhang, T.; Winey, K. I.; Riggleman, R. A. Polymer Conformations and Dynamics under Confinement with Two Length Scales. *Macromolecules* **2019**, *52* (1), 217–226.

- https://doi.org/10.1021/acs.macromol.8b01779.
- (48) Luna, F. V.; Maurya, A. K.; de Souza e Silva, J. M.; Dittrich, G.; Paul, T.; Enke, D.; Huber, P.; Wehrspohn, R.; Steinhart, M. Straight versus Spongy: Effect of Tortuosity on Polymer Imbibition into Nanoporous Matrices Assessed by Segmentation-Free Analysis of 3D Sample Reconstructions. *J. Phys. Chem. C* 2022, 126 (30), 12765–12779. https://doi.org/10.1021/acs.jpcc.2c01991.
- (49) Rubinstein, M.; Colby, R. H. *Polymer Physics*; Oxford University Press: Oxford; New York, 2003.
- (50) Ding, Y.; Kim, Y.-J.; Erlebacher, J. Nanoporous Gold Leaf: Ancient Technology Advanced Material. *Adv. Mater.* **2004**, *16* (21), 1897–1900. https://doi.org/10.1002/adma.200400792.
- (51) Ng, A. K.; Welborn, S. S.; Detsi, E. Time-Dependent Power Law Function for the Post-Dealloying Chemical Coarsening of Nanoporous Gold Derived Using Small-Angle X-Ray Scattering. *Scr. Mater.* **2022**, *206*, 114215. https://doi.org/10.1016/j.scriptamat.2021.114215.
- (52) Welborn, S. S.; Detsi, E. Small-Angle X-Ray Scattering of Nanoporous Materials. *Nanoscale Horiz.* **2020**, *5* (1), 12–24. https://doi.org/10.1039/C9NH00347A.
- (53) Welborn, S. S.; Van Der Meer, S.; Corsi, J. S.; De Hosson, J. Th. M.; Detsi, E. Using X-Ray Scattering to Elucidate the Microstructural Instability of 3D Bicontinuous Nanoporous Metal Scaffolds for Use in an Aperiodic 3D Tricontinuous Conductor–Insulator–Conductor Nanocapacitor. ACS Appl. Mater. Interfaces 2021, 13 (10), 11721–11731. https://doi.org/10.1021/acsami.0c16869.
- (54) Boerner, T. J.; Deems, S.; Furlani, T. R.; Knuth, S. L.; Towns, J. ACCESS: Advancing Innovation: NSF's Advanced Cyberinfrastructure Coordination Ecosystem: Services & Support. In *Practice and Experience in Advanced Research Computing*; PEARC '23; Association for Computing Machinery: New York, NY, USA, 2023; pp 173–176. https://doi.org/10.1145/3569951.3597559.
- (55) Plimpton, S. Fast Parallel Algorithms for Short-Range Molecular Dynamics. *J. Comput. Phys.* **1995**, *117* (1), 1–19. https://doi.org/10.1006/jcph.1995.1039.
- (56) Kremer, K.; Grest, G. S. Dynamics of Entangled Linear Polymer Melts: A Molecular-dynamics Simulation. J. Chem. Phys. 1990, 92 (8), 5057–5086. https://doi.org/10.1063/1.458541.
- (57) Kumar, R.; Goswami, M.; Sumpter, B. G.; Novikov, V. N.; Sokolov, A. P. Effects of Backbone Rigidity on the Local Structure and Dynamics in Polymer Melts and Glasses. *Phys. Chem. Chem. Phys.* **2013**, *15* (13), 4604–4609. https://doi.org/10.1039/C3CP43737J.
- (58) Mavrantzas, V. G.; Boone, T. D.; Zervopoulou, E.; Theodorou, D. N. End-Bridging Monte Carlo: A Fast Algorithm for Atomistic Simulation of Condensed Phases of Long Polymer Chains. *Macromolecules* **1999**, *32* (15), 5072–5096. https://doi.org/10.1021/ma981745g.
- (59) Banaszak, B. J.; de Pablo, J. J. A New Double-Rebridging Technique for Linear Polyethylene. *J. Chem. Phys.* **2003**, *119* (4), 2456–2462. https://doi.org/10.1063/1.1583673.
- (60) Hu, K.; Ziehmer, M.; Wang, K.; Lilleodden, E. T. Nanoporous Gold: 3D Structural Analyses of Representative Volumes and Their Implications on Scaling Relations of Mechanical Behaviour. *Philos. Mag.* **2016**, 96 (32–34), 3322–3335. https://doi.org/10.1080/14786435.2016.1222087.
- (61) Lilleodden, E. T.; Voorhees, P. W. On the Topological, Morphological, and Microstructural Characterization of Nanoporous Metals. *MRS Bull.* **2018**, *43* (1), 20–26. https://doi.org/10.1557/mrs.2017.303.
- (62) Wittstock, A.; Biener, J.; Bäumer, M. Nanoporous Gold: A New Material for Catalytic and Sensor Applications. *Phys. Chem. Chem. Phys.* **2010**, *12* (40), 12919. https://doi.org/10.1039/c0cp00757a.

- (63) Michels, A.; Weissmüller, J. Magnetic-Field-Dependent Small-Angle Neutron Scattering on Random Anisotropy Ferromagnets. *Rep. Prog. Phys.* **2008**, *71* (6), 066501. https://doi.org/10.1088/0034-4885/71/6/066501.
- (64) Li, Y.; Pham, J. Q.; Johnston, K. P.; Green, P. F. Contact Angle of Water on Polystyrene Thin Films: Effects of CO ₂ Environment and Film Thickness. *Langmuir* **2007**, 23 (19), 9785–9793. https://doi.org/10.1021/la0636311.
- (65) Erb, R. The Wettability of Gold. The Journal of Physical Chemistry 1967, 2412–2413.
- (66) Fox, T. G.; Flory, P. J. Viscosity—Molecular Weight and Viscosity—Temperature Relationships for Polystyrene and Polyisobutylene ^{1,2}. *J. Am. Chem. Soc.* **1948**, *70* (7), 2384–2395. https://doi.org/10.1021/ja01187a021.
- (67) Colby, R. H.; Fetters, L. J.; Graessley, W. W. The Melt Viscosity-Molecular Weight Relationship for Linear Polymers. *Macromolecules* **1987**, *20* (9), 2226–2237. https://doi.org/10.1021/ma00175a030.
- (68) Masoodi, R.; Pillai, K. M.; Varanasi, P. P. Darcy's Law-Based Models for Liquid Absorption in Polymer Wicks. *AIChE J.* **2007**, *53* (11), 2769–2782. https://doi.org/10.1002/aic.11322.
- (69) Luo, J.-W.; Chen, L.; Min, T.; Shan, F.; Kang, Q.; Tao, W. Macroscopic Transport Properties of Gyroid Structures Based on Pore-Scale Studies: Permeability, Diffusivity and Thermal Conductivity. *Int. J. Heat Mass Transf.* 2020, 146, 118837. https://doi.org/10.1016/j.ijheatmasstransfer.2019.118837.
- (70) Kröger, M.; Dietz, J. D.; Hoy, R. S.; Luap, C. The Z1+ Package: Shortest Multiple Disconnected Path for the Analysis of Entanglements in Macromolecular Systems. *Comput. Phys. Commun.* **2023**, 283, 108567. https://doi.org/10.1016/j.cpc.2022.108567.
- (71) Tarnacka, M.; Talik, A.; Kamińska, E.; Geppert-Rybczyńska, M.; Kaminski, K.; Paluch, M. The Impact of Molecular Weight on the Behavior of Poly(Propylene Glycol) Derivatives Confined within Alumina Templates. *Macromolecules* 2019, 52 (9), 3516–3529. https://doi.org/10.1021/acs.macromol.9b00209.
- (72) Lin, E. Y.; Frischknecht, A. L.; Winey, K. I.; Riggleman, R. A. Effect of Surface Properties and Polymer Chain Length on Polymer Adsorption in Solution. *J. Chem. Phys.* **2021**, *155* (3), 034701. https://doi.org/10.1063/5.0052121.
- (73) O'Shaughnessy, B.; Vavylonis, D. Non-Equilibrium in Adsorbed Polymer Layers. *J. Phys. Condens. Matter* **2004**, *17* (2), R63. https://doi.org/10.1088/0953-8984/17/2/R01.
- (74) Zhao, J.; Granick, S. How Polymer Surface Diffusion Depends on Surface Coverage. *Macromolecules* **2007**, *40* (4), 1243–1247. https://doi.org/10.1021/ma062104I.
- (75) Lin, E. Y.; Frischknecht, A. L.; Riggleman, R. A. Chain and Segmental Dynamics in Polymer–Nanoparticle Composites with High Nanoparticle Loading. *Macromolecules* **2021**, *54* (12), 5335–5343. https://doi.org/10.1021/acs.macromol.1c00206.
- (76) Lin, E. Y.; Frischknecht, A. L.; Riggleman, R. A. Origin of Mechanical Enhancement in Polymer Nanoparticle (NP) Composites with Ultrahigh NP Loading. *Macromolecules* **2020**, 53 (8), 2976–2982. https://doi.org/10.1021/acs.macromol.9b02733.